Carbohydrate Polymers 379 (2026) 124970

Contents lists available at ScienceDirect

Carbohydrate Polymers

journal homepage: www.elsevier.com/locate/carbpol

Preparation of nanoparticles from atmospheric pressure plasma jet-activated gas modified pectin for oral insulin delivery

Nuo Chen [a], Xijia Zhang [b], Weichao Cao [a], Hong Tian [c], Xiao Hua [a,*]

[a] School of Food Science and Technology, Jiangnan University, Wuxi, 214122, China
[b] Academy of Contemporary Food Engineering, South China University of Technology, Guangzhou Higher Education Mega Center, Guangzhou, 510006, China
[c] School of Food Technology and Natural Sciences, Massey University, Palmerston North, New Zealand

ARTICLE INFO

Keywords:
Pectin
Atmospheric pressure plasma jet-activated gas
Nanoparticles
Oral insulin delivery
Transepithelial transport

ABSTRACT

This study investigates the effects of atmospheric pressure plasma jet-activated gas (APPJ) treatment on pectin and its nanoparticles (APPJ-pectin NPs), and explores their applications in oral insulin delivery systems. The results showed that as APPJ treatment progressed, the molecular weight of pectin significantly decreased, while the degree of esterification increased and its hydrophilic/hydrophobic properties altered. The insulin encapsulation efficiency of APPJ-pectin NPs exhibited minimal variation during the initial stage of treatment. In vitro release studies showed that APPJ-pectin NPs protected insulin in simulated gastric fluid and gradually released it at neutral pH, with the release rate initially decreasing and then increasing with extended APPJ treatment. The hemolysis rates of all samples ranged from 2% to 5%, suggesting that APPJ-pectin NPs exhibited favorable hemocompatibility. APPJ-pectin NPs primarily underwent transepithelial transport via the transcellular pathway, being internalized by endocytosis and subsequently transported intracellularly into the bloodstream. The transepithelial transport efficiency of APPJ-pectin NPs was evaluated using the Transwell system. APPJ treatment significantly increased the transport efficiency, with A60-NPs showing a 57.14% increase compared to the control. Confocal laser scanning microscope observations and flow cytometry experiments further confirmed this result, demonstrating that the uptake of APPJ-pectin NPs by Caco-2 cells was time-dependent, with A60-NPs exhibiting the highest uptake efficiency.

1. Introduction

Diabetes mellitus is a chronic metabolic disease with a high global prevalence, characterized by persistent hyperglycemia. Prolonged dysglycemia leads to a wide range of complications, thereby posing a significant threat to patient health. According to estimates for 2025 from the International Diabetes Federation (IDF), the global number of clinically diagnosed type 1 diabetes (T1D) cases has reached 9.5 million, representing a 13% increase relative to 2021. Notably, low-income countries recorded growth rates of up to 20% (Ogle et al., 2025). These data underscore the escalating global burden of T1D and highlight the substantial public health challenges arising from inequitable medical resource distribution. As the therapeutic cornerstone for T1D and for a subset of T2D, exogenous insulin is indispensable for achieving optimal glycemic control and for mitigating diabetes-related complications when administered appropriately. However, in current clinical practice, insulin therapy remains largely reliant on subcutaneous injection, a route that often compromises patient adherence and is associated with local discomfort, inflammation, and an elevated risk of infection (Wang, Sun, & Mu, 2024; Zheng et al., 2025). Consequently, the development of non-injectable insulin delivery systems, particularly oral formulations that offer greater patient acceptability, has become a major focus and persistent challenge in contemporary diabetes research. However, as a protein therapeutic, insulin is highly vulnerable to degradation by gastric acid and enzymatic hydrolysis in the gastrointestinal tract (Low et al., 2025). In addition, its large molecular size and strong hydrophilicity significantly hinder its ability to traverse the intestinal epithelium and mucus barrier, leading to poor systemic absorption and extremely low oral bioavailability (Wang et al., 2024). Collectively, these physiological barriers severely constrain the feasibility of oral insulin delivery in clinical practice.

Substantial progress has been made in the development of oral insulin delivery systems, with common carriers including polymeric nanoparticles, liposomes, metal-organic frameworks (MOFs), and silica

* Corresponding author.
E-mail address: huaxiao@jiangnan.edu.cn (X. Hua).

https://doi.org/10.1016/j.carbpol.2026.124970
Received 3 November 2025; Received in revised form 4 January 2026; Accepted 19 January 2026
Available online 23 January 2026

nanoparticles (Zou et al., 2025). These delivery systems can partially protect insulin from gastric acid and enzymatic degradation while concurrently enhancing its transport across the intestinal epithelial barrier. For example, the oral insulin formulation ORMD-0801 developed by Oramed utilizes enzyme inhibitors and permeation enhancers to facilitate absorption. Although it advanced to Phase III clinical trials, it ultimately failed to show superiority over placebo in lowering blood glucose levels, raising concerns about its inconsistent efficacy (Zhang, Zhu, Song, Shi, & Cao, 2024). In addition, 50 nm negatively charged silica nanoparticles are capable of temporarily opening epithelial tight junctions to enhance insulin absorption. Nonetheless, their non-biodegradable nature raises concerns that require comprehensive long-term safety evaluation (Lamson, Berger, Fein, & Whitehead, 2020). Consequently, most existing delivery systems remain limited by inadequate physicochemical stability, poorly controlled release kinetics, and a paucity of long-term safety data. Against this backdrop, nanoparticle delivery systems fabricated from natural polymers are drawing growing interest owing to their superior biocompatibility, structural tunability, and strong intestinal mucoadhesiveness.

Pectin, a naturally derived polysaccharide, has attracted widespread attention as an ideal material for oral delivery systems because of its favorable physicochemical properties, including biodegradability, biocompatibility, and pH-responsive behavior (Pei et al., 2024). In recent years, pectin-based nanoparticles have made noteworthy strides in drug delivery research. By forming nanoscale carrier architectures, they help preserve drug activity and improve bioavailability. Gu, Li, Jiang, Chang, and Wu (2024) prepared whey protein/zein composite nanoparticles coated with pectin by first adjusting the pH and then applying heat to induce electrostatic adsorption. The resulting nanoparticles exhibited outstanding structural stability, high tolerance to simulated gastrointestinal conditions, and excellent dispersibility in aqueous media. These nanoparticles demonstrate excellent controlled release performance for curcumin, help preserve its antioxidant activity, and retain good redispersibility after drying, highlighting their potential as oral delivery carriers. However, despite its many intrinsic advantages, unmodified pectin still faces practical limitations, including relatively low drug loading capacity and inadequate structural stability under complex physiological conditions that often lead to premature drug release and reduced delivery efficiency.

Atmospheric pressure plasma jet-activated gas (APPJ) technology generates cold plasma under ambient conditions. When an electric field is applied, gas molecules or atoms are excited and ionized, yielding highly reactive oxygen and nitrogen species (RONS) (Seelarat et al., 2024). RONS are classified into long-lived reactive species (such as H_2O_2, O_3, and NO_3^-) and short-lived radical species (such as •OH, NO•, and O_2^-) based on their lifetimes (Lv, Shang, Lu, Yang, & Guo, 2025; Shang, Morent, De Geyter, Wang, & Yang, 2025). These RONS play a crucial role in the plasma-induced polysaccharide modification process. They interact with the polysaccharide molecular chains through oxidation reactions, thereby modifying the physicochemical properties of the polysaccharides, such as molecular weight, molecular structure, bioactivity, viscosity, and hydrophilicity/hydrophobicity (Fang, Yang, Liu, Shao, & Zhang, 2013). Matra et al. (2023) used the Electrical Breakdown in Liquid (EBL) process to treat inulin and found that plasma treatment significantly degraded the polysaccharide structure of inulin. After treatment, the inulin, originally in a micro spherical shape, was transformed into fragmented particles. The DPPH radical scavenging assay demonstrated that the plasma-treated inulin exhibited a 311% increase in antioxidant activity compared to the untreated inulin. RONS can also introduce functional groups, such as carboxyl and hydroxyl groups (Booth, Mozetic, Nikiforov, & Oehr, 2022), onto the polysaccharide molecules, thereby imparting new characteristics and application potential to the polysaccharides. Overall, plasma treatment significantly enhances the application potential of polysaccharides in fields such as biomedicine, the food industry, and environmental management. For example, Surucu, Masur, Sasmazel, Von Woedtke, and Weltmann (2016) used APPJ, driven by either argon or air, to modify the surface of electrospun PCL/chitosan/PCL hybrid scaffolds. The APPJ-treated scaffolds exhibited improved hydrophilicity, along with the incorporation of oxygen and nitrogen functional groups on the surface. These modifications enhanced the scaffold's biocompatibility and promoted the attachment and proliferation of fibroblasts (MRC-5 cells) on its surface. Moreover, RONS demonstrate potent antimicrobial and bactericidal activities, facilitating surface disinfection and promoting cellular repair in medical and biomedical applications. In contrast to traditional chemical or enzymatic modifications, APPJ offers a non-contact, non-thermal, and environmentally friendly approach for modification, enabling precise structural regulation of natural polysaccharides while preserving their biocompatibility.

Pectin's pH-responsive properties enable it to protect drugs from gastric degradation and release them in neutral pH regions, making it a promising candidate for oral insulin delivery. However, the ability of pectin-based oral delivery systems to facilitate transepithelial transport remains unclear. Previous studies have primarily focused on enhancing their stability through chemical modifications or crosslinking reactions—methods that are often associated with complex reaction conditions, chemical residues, and reduced biocompatibility, thereby limiting their further application in the biomedical field. In this context, we hypothesize that APPJ treatment could serve as a controllable and environmentally friendly modification strategy, inducing changes in the molecular weight, degree of esterification, and molecular structure of pectin without introducing chemical residues, thereby modulating its physicochemical properties such as hydrophilicity/hydrophobicity, surface charge, gelation ability, and adhesiveness. These changes are expected to enhance the encapsulation efficiency, stability under complex physiological conditions, drug release properties, and transepithelial transport efficiency of pectin-based nanoparticles. This study contributes to elucidating the mechanism by which APPJ regulates the structure of natural polysaccharides and provides new insights into the development of efficient and sustainable oral insulin delivery systems. To validate this hypothesis, the structure and physicochemical properties of the APPJ-modified pectin (APPJ-pectin) were thoroughly analyzed through MW determination, FTIR, NMR, rheological analysis, and contact angle measurement. APPJ-pectin was used to develop an oral insulin nanoparticles delivery system. The system's potential for oral insulin delivery was evaluated, including particle size, Zeta potential, insulin encapsulation efficiency, SEM morphology, in vitro insulin release behavior, biocompatibility assessment, transepithelial transport studies, and Caco-2 cell uptake experiments.

2. Materials and methods

2.1. Materials

Natural pectin (purity ≥99%, weight average molecular weight = 483 kDa, degree of esterification = 57.44%, monosaccharide composition: Fuc, 2.43%; Rha, 8.05%; Ara, 3.34%; Gal, 25.94%; Glc, 3.79%; Xyl, 1.16%; GalA, 55.29%) was purchased from Sigma-Aldrich Co., Ltd. (St. Louis, USA). Recombinant human insulin (purity ≥99%) and deuterium oxide (D_2O, purity ≥99%) were purchased from MERYER Co., Ltd. (Shanghai, China). Fresh whole blood of Sprague–Dawley rats (SD rats) was obtained from SiPeiFu Biotechnology Co., Ltd. (Beijing, China). Human insulin ELISA kit (B75453-96 T) was obtained from MERYER Co., Ltd. (Shanghai, China).

2.2. APPJ treatment of pectin

A natural pectin solution (4 mg/mL) was treated using an APPJ device (XJ-DW-5, Xianjing Plasma Technology Institute Co., Ltd., China). The APPJ nozzle was connected to the reaction vessel via an inert hose, with the end of the hose inserted into the pectin solution (Fig. 1a). The plasma was then ignited, and the gas flow stabilized to allow the jet

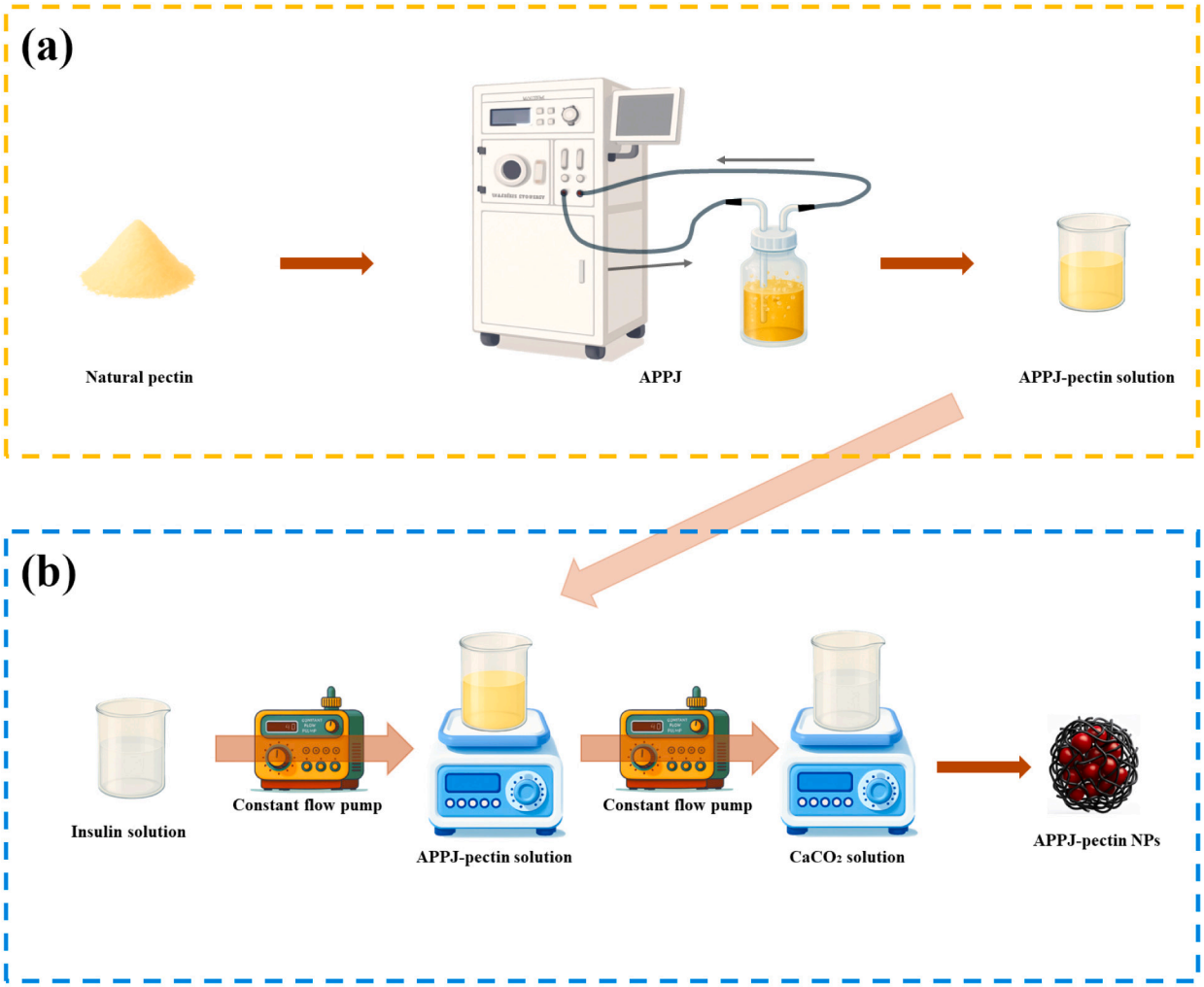

Fig. 1. Schematic of the APPJ treatment of pectin (a) and the preparation of APPJ-pectin nanoparticles (b).

products to continuously pass into the solution (Sangwanna et al., 2023). The flow rate of the plasma-activated gas introduced into the pectin solution was controlled to maintain a continuous boiling state. After every 10 min treatment, the solution was shaken to ensure uniform mixing, thereby ensuring that the pectin solution was evenly exposed to the APPJ treatment. Samples were collected at 0, 30, 60, 90, and 120 min, with 0 min as the control. The reaction vessel was placed in an ice bath to control the temperature during the treatment. The operating conditions were as follows: gas type, air; gas flow rate, 10 L/min; power, 150 W; voltage, 380 V. According to the APPJ treatment time, the samples were designated as Control, A30-Pectin, A60-Pectin, A90-Pectin, and A120-Pectin.

2.3. Preparation of APPJ-pectin nanoparticles (NPs)

A 10 mL insulin solution (500 μg/mL, pH 3.0) was slowly added (1 mL/min) to 20 mL of either natural pectin (Control) or APPJ-pectin solution (4.0 mg/mL) using a constant flow pump. The mixture was continuously stirred on a magnetic stirrer (200 rpm) during the addition. After the complete addition of insulin, the mixture was stirred for an additional 10 min. The insulin-pectin solution was then pumped at the same flow rate into 20 mL of $CaCl_2$ solution (2.0 mg/mL), while maintaining stirring (Fig. 1b). The mixture was further stirred at room temperature for 2 h to facilitate the formation of APPJ-pectin NPs. The suspension was then subjected to 2 min of ultrasonication (amplitude 30%, maximum power 1200 W) to reduce aggregation. The APPJ-pectin NPs suspension was washed twice with distilled water (pH 4.0) by centrifugation at 6600 rpm for 20 min at 4 °C, and subsequently resuspended in an equal volume of distilled water (pH 4.0) to obtain the APPJ-pectin NPs samples. Some of the samples were stored at 4 °C, while the remaining samples were freeze-dried for future use. The samples were labeled as Control, A30-NPs, A60-NPs, A90-NPs, and A120-NPs, according to the type of pectin solution used.

2.4. Preparation of APPJ-pectin-fluorescein isothiocyanate (FITC) NPs

50 mg of FITC was dissolved in 10 mL of DMSO and then added dropwise to 100 mL of Na_2CO_3 buffer (0.1 M Na_2CO_3, 0.2 M EDTA, pH 9.0) containing 250 mg of insulin. The mixture was stirred at room temperature for 12 h in the dark. After the reaction, NH_4Cl solution was added to terminate the reaction, and the mixture was transferred into a dialysis bag (3.5 kDa) and dialyzed against phosphate buffer (pH 7.2) until the dialysate became colorless (Elsabahy et al., 2021; Nabila et al., 2024). After dialysis, the solution was aliquoted and frozen in liquid nitrogen, followed by freeze-drying to obtain FITC-labeled insulin (ins-FITC), which was stored at −20 °C in the dark.

10 mg of FITC was dissolved in 2 mL of DMSO and then diluted with ultrapure water to a final volume of 100 mL. The solution was then diluted with ultrapure water to obtain FITC standard solutions at concentrations of 15 μg/mL, 7.5 μg/mL, 3.75 μg/mL, 1.88 μg/mL, 0.94 μg/mL, 0.47 μg/mL, and 0 μg/mL. 200 μL of each FITC standard solution and ins-FITC solution (0.5 mg/mL) were added to a 96-well plate, and

the fluorescence intensity was measured using a microplate reader with excitation and emission wavelengths set at 490 nm and 520 nm, respectively. A standard curve was plotted based on the measured fluorescence intensity, and the FITC labeling efficiency was calculated accordingly. The labeling efficiency was defined as the mass ratio of FITC to the labeled insulin.

APPJ-pectin-FITC NPs were prepared following the method described in Section 2.3, with insulin replaced by ins-FITC while keeping the other procedures unchanged.

2.5. Particle size and zeta potential of APPJ-pectin NPs

The particle size and Zeta potential of APPJ-pectin NPs were characterized using a dynamic light scattering (DLS) instrument (NanoBrook Omni, Brookhaven Instruments Corporation, USA). The parameters were set as follows: scattering angle, 90°; refractive index, 1.46; measurement temperature, 25 °C; equilibration period, 2 min.

2.6. Insulin encapsulation efficiency of APPJ-pectin NPs

The APPJ-pectin NPs suspension was centrifuged at 11,500 rpm for 20 min at 4 °C. The insulin concentration in the supernatant was determined using an insulin ELISA kit (B75453-96 T, MERYER, China). The calculation formula for insulin encapsulation efficiency was as follows (Huo et al., 2023):

$$\text{Encapsulation efficiency}\ (\%) = \frac{\text{Total ins} - \text{Free ins}}{\text{Total ins}} \times 100\%$$

Total ins: the total mass of insulin added during the preparation of APPJ-pectin NPs; Free ins: the total mass of insulin in the supernatant.

2.7. In vitro simulated insulin release of APPJ-pectin NPs

The in vitro simulated insulin release test for the APPJ-pectin NPs samples was modified from the method detailed by Zhu et al. (2024). APPJ-pectin NPs samples were mixed in equal proportions with simulated gastric fluid (SGF, pH 1.2, 0.2% (*w/v*) NaCl, and 0.1% (w/v) pepsin, 3000 U/mg). The mixture was incubated at 37 °C with shaking (150 rpm) for 2 h. At predetermined time intervals, 2 mL of the incubated mixture was withdrawn and centrifuged at 11,500 rpm for 10 min at 4 °C to remove the supernatant. The precipitate was washed twice with distilled water (pH 4) to remove residual pepsin. 2 mL of standard pH buffer solution (pH 9) was added to the precipitate and incubated at 37 °C with shaking until complete dissolution of the precipitate. The insulin concentration in the solution (unreleased insulin) was determined using an insulin ELISA kit. The insulin release rate was calculated using the following formula:

$$\text{Release rate}\ (\%) = \frac{\text{Total ins} - \text{Unreleased ins}}{\text{Total ins}} \times 100\%$$

After incubation in SGF, the APPJ-pectin NPs samples were mixed in equal proportions with simulated intestinal fluid (SIF, pH 7.4, 0.1% (*w/v*) $CaCl_2$, 1.0% (w/v) bile salts, 0.2% (w/v) Tris, and 0.1% (w/v) trypsin, 130 U/mg). The mixture was incubated at 37 °C with shaking (150 rpm). At predetermined time intervals, 2 mL of the incubated mixture was withdrawn for analysis. The treatment of the mixed samples, the determination of insulin concentration, and the calculation of insulin release rate were performed as described above.

2.8. Circular dichroism (CD) spectroscopy of natural and released insulin

The dissolved insulin solution was added to a standard pH buffer solution at pH 7.4 to obtain the natural insulin sample. The APPJ-pectin NPs samples were incubated in a standard pH buffer solution at pH 7.4 with shaking at 37 °C for 10 h to obtain the released insulin samples.

The protein structural characteristics of insulin were analyzed using a circular dichroism (CD) spectrometer (MOS-450, BIO-Logic, France). All measurements were conducted at a constant temperature of 25 °C, and baseline correction was performed using the corresponding buffer blanks. Measurements were performed in the far UV (190–250 nm) and near UV (250–320 nm) wavelength ranges, using quartz cuvettes with path lengths of 0.1 cm and 1.0 cm, respectively. The scanning parameters were set as follows: bandwidth, 1.0 nm; data interval, 1.0 nm; scanning speed, 50 nm/min.

2.9. Hemocompatibility assessment of APPJ-pectin NPs

The hemocompatibility of APPJ-pectin NPs was evaluated with modifications according to the method described by Libo et al. (2024). Freshly collected SD rat blood was centrifuged at 4200 rpm for 10 min at 4 °C to remove the supernatant, and the pellet was repeatedly washed with 0.01 M PBS until the supernatant became clear. The supernatant was removed to obtain a red blood cell suspension. The red blood cell suspension was diluted with 20 volumes of 0.01 M PBS. APPJ-pectin NPs samples were dispersed in PBS to prepare a solution with a concentration of 1 mg/mL. 0.2 mL diluted red blood cell suspension was added to 0.8 mL of PBS (negative control), 0.8 mL of distilled water (positive control), and 0.8 mL of APPJ-pectin NPs suspension, respectively. After incubation at 37 °C with shaking (150 rpm) for 2 h, the mixture was centrifuged at 4200 rpm for 10 min at 4 °C. The absorbance of the supernatant at 540 nm was measured using a spectrophotometer. The hemolysis rate was calculated using the following formula:

$$\text{Hemolysis rate}\ (\%) = \frac{A_s - A_n}{A_p - A_n} \times 100\%$$

A_s: absorbance of the sample; A_n: absorbance of the negative control; A_p: absorbance of the positive control.

2.10. Transepithelial transport study of APPJ-pectin NPs in vitro

Caco-2 cells were seeded at a density of 1.2×10^5 cells onto the apical chamber (AP) of 12-well Transwell inserts with a seeding volume of 0.5 mL, while 1.0 mL of complete medium was added to the basolateral chamber (BL). After seeding, the cells were cultured at 37 °C in an atmosphere containing 5% CO_2, and the medium replaced every two days. After one week, the medium was replaced daily. Transepithelial electrical resistance (TEER) was measured using a Millicell-ERS voltmeter to evaluate the differentiation and maturation of the cell monolayer. After 21 days of culture, a TEER greater than 500 $\Omega \cdot cm^2$ was considered indicative of a fully formed cell monolayer with an intact barrier, which was used for subsequent experiments (Yang et al., 2025; Yuan et al., 2024). TEER was calculated using the following formula:

$$\text{TEER} = (R_s - R_b) \times A$$

Rs: the resistance value of the Transwell polycarbonate membrane with cells seeded; Rb: the resistance value of the Transwell polycarbonate membrane without cells; A: the effective membrane area (1.13 cm^2) of the 12-well Transwell insert.

After 21 days of culture on Transwell inserts, the culture medium on both the AP and BL was removed, and the cells were washed three times with Hank's Balanced Salt Solution (HBSS). Subsequently, 0.5 mL of HBSS containing APPJ-pectin-FITC NPs was added to the AP, while 1.0 mL of HBSS was added to the BL. At 30, 60, and 90 min, 200 μL of sample solution was withdrawn from the BL and replaced with an equal volume of prewarmed HBSS. The concentration of ins-FITC in the collected samples was measured using a fluorescence microplate reader. The apparent permeability coefficient (Papp) was calculated using the following equation (Yang et al., 2023):

$$P_{app} = \frac{d_Q}{d_t} \times \frac{1}{A \times C_0}$$

dQ/dt: amount of ins-FITC transported per unit time (μg/s); A:

effective membrane area of the 12-well Transwell insert (1.13 cm^2); C_0: initial concentration of ins-FITC (μg/mL).

2.11. Morphological observation of Caco-2 cells

Caco-2 cells were seeded in glass-bottom culture dishes and cultured according to the method described in Section 2.10. Caco-2 cells were examined and imaged under an optical microscope at days 2, 4, 7, 11, 15, and 21 to evaluate their growth throughout the transepithelial transport study.

2.12. Scanning electron microscopy (SEM) analysis of APPJ-pectin NPs

10 μL of the ultrasonically treated APPJ-pectin NPs was dropped onto a silicon wafer and quickly dried in a vacuum oven at 40 °C. After drying, the sample on the silicon wafer was coated with gold by sputtering. The microstructure of APPJ-pectin NPs was analyzed using a SEM (S-4800-I, Hitachi, Japan).

2.13. Evaluation of APPJ-pectin NPs uptake by Caco-2 cells

2.13.1. Confocal laser scanning microscope (CLSM) observation

Caco-2 cells were seeded in glass-bottom culture dishes at a density of 1×10^5 cells and cultured at 37 °C in an atmosphere containing 5% CO_2. When the cells reached approximately 70% confluence, the culture medium was replaced with fresh medium containing APPJ-pectin-FITC NPs, and the cells were further incubated for 2 h. After incubation, the cells were washed three times with PBS and fixed with 4% paraformaldehyde for 15 min. Subsequently, the cells were washed three times with PBS, stained with DAPI for 5 min to label the nuclei, and then washed three times with PBS again (Joshi et al., 2025). The culture dishes were observed under a CLSM with excitation wavelengths of 405 nm and 488 nm.

2.13.2. Flow cytometric analysis

Caco-2 cell culture was performed as described in Section 2.13.1. When the cells reached approximately 80% confluence, the culture medium was replaced with fresh medium containing APPJ-pectin-FITC NPs, and the cells were further incubated for 0, 0.5, and 1.5 h. After incubation, the cells were washed three times with PBS. The cells were detached by adding trypsin solution and centrifuged at 1800 rpm for 5 min. The cell pellet was resuspended in 500 μL PBS. The uptake of APPJ-pectin-FITC NPs by Caco-2 cells was analyzed using a spectral flow cytometer (SA3800, Sony, Japan), and the data were processed with FlowJo software (BD Biosciences, USA) (Shiyang et al., 2024).

2.14. Analysis of the transepithelial transport mechanism of APPJ-pectin NPs

2.14.1. TEER measurement in Caco-2 cell monolayers

Caco-2 cells were cultured for 21 days to form a cell monolayer, following the method described in Section 2.10. The culture medium in the AP was replaced with fresh medium containing APPJ-pectin NPs, and the cells were incubated for 2 h. After incubation, the cells were washed three times with HBSS. Fresh medium was then added to both the AP and BL chambers. The TEER of the samples was continuously measured over the next 10 h.

2.14.2. Immunofluorescence staining of tight junction protein zonula Occludens-1 (ZO-1)

Caco-2 cells were seeded in glass-bottom dishes and cultured as described in Section 2.10. After the cells formed a monolayer over 21 days, the medium was replaced with fresh medium containing APPJ-pectin NPs and incubated for 2 h. Samples without APPJ-pectin NPs treatment served as the control (untreated).

After incubation, the cells were washed three times with PBS, then fixed with fixation solution (P0098) for 10 min. After fixation, the cells were washed three times with washing solution (P0106), each for 5 min. Blocking solution (P0102) was added and incubated at room temperature for 1 h, followed by three washes. Then, diluted ZO-1 Rabbit Polyclonal Antibody (AF0321) was added, and the cells were incubated overnight at 4 °C. After incubation, the cells were washed three times. Then, diluted AF488-labeled Goat Anti-Rabbit IgG (H + L) (A0423) was added, and the cells were incubated at room temperature for 1 h, followed by three washes. Finally, the cells were stained with mounting solution (P0131) for 5 min. Immunofluorescence staining results were observed using CLSM at 405 nm and 488 nm wavelengths. All reagents for immunofluorescence staining were purchased from Beyotime Co., Ltd. (Shanghai, China).

2.14.3. Co-localization of endoplasmic reticulum (ER) and APPJ-pectin-FITC NPs in Caco-2 cells

Caco-2 cell culture and APPJ-pectin-FITC NPs treatment were performed according to the method described in Section 2.13.1. After treatment, the cells were washed three times with HBSS. Then, ER-Tracker Red solution (C1041S, Beyotime, China) was added, and the cells were incubated for 30 min. Finally, the mounting solution containing DAPI was added, and the samples were observed using CLSM at 405, 488, and 552 nm wavelengths.

3. Results and discussion

3.1. Characterization of APPJ-pectin

3.1.1. Weight average molecular weight (MW) of APPJ-pectin

The effect of APPJ treatment on the weight average molecular weight of APPJ-pectin is shown in Fig. 2 and Table 1. After APPJ treatment, all APPJ-pectin MW chromatograms showed a single peak with no other significant peaks, and the peak shape was similar to that of the control group. These results indicated that APPJ treatment led to a uniform decrease in the MW of pectin, indirectly suggested that the modification effect of APPJ on pectin was uniform. The MW of natural pectin in the control group was 483,417 Da. With prolonged treatment time, a significant decrease in the MW was observed, reaching 358,297 Da of A30-Pectin, 260,936 Da of A60-Pectin, 199,776 Da of A90-Pectin, and 142,557 Da of A120-Pectin. These results indicated that APPJ treatment effectively induced the degradation of the pectin backbone. A 30-min treatment reduced the MW of natural pectin by approximately 26%, and a 120-min treatment reduced it by more than 70%. In the solution treated with APPJ, the pH and electrical conductivity of the APPJ-pectin solution changed (Table S1), suggesting the generation of RONS and their effective incorporation into the solution (Table S2). These RONS, such as O_3, H_2O_2, ·OH, NO_2^-,and ·NO, were able to cleave the glycosidic linkages (Liu et al., 2023). For example, Chokradjaroen et al. (2017) found that ·OH radicals attacked the C-1 carbon of chitosan, transferring the radical to this carbon by removing the hydrogen atom from it, which broke the β-1,4 glycosidic bond of chitosan and reduced its MW. On the other hand, plasma-generated electrons directly cleaved the β-1,4 glycosidic bond of chitosan, further decreasing its MW. By comparing the concentrations of RONS in APPJ-treated water and the APPJ-pectin solution, it was inferred that H_2O_2 and NO_2^- were likely the primary long-lived RONS responsible for mediating pectin modification. Hu et al. (2023) treated pectin with solution pulsed plasma (2.4 kV) for 60 min, reducing its MW from 356.5 kDa to 60.53 kDa.

3.1.2. FTIR spectrum of APPJ-pectin

FTIR analyzes the molecular structure of dried materials by measuring the characteristic absorption of infrared light (moisture has strong absorption in the infrared spectral region), and is commonly used to investigate the functional group changes of polysaccharides after plasma treatment. The FTIR spectrum is shown in Fig. 3a. The APPJ treatment significantly affected the degree of esterification (DE) of

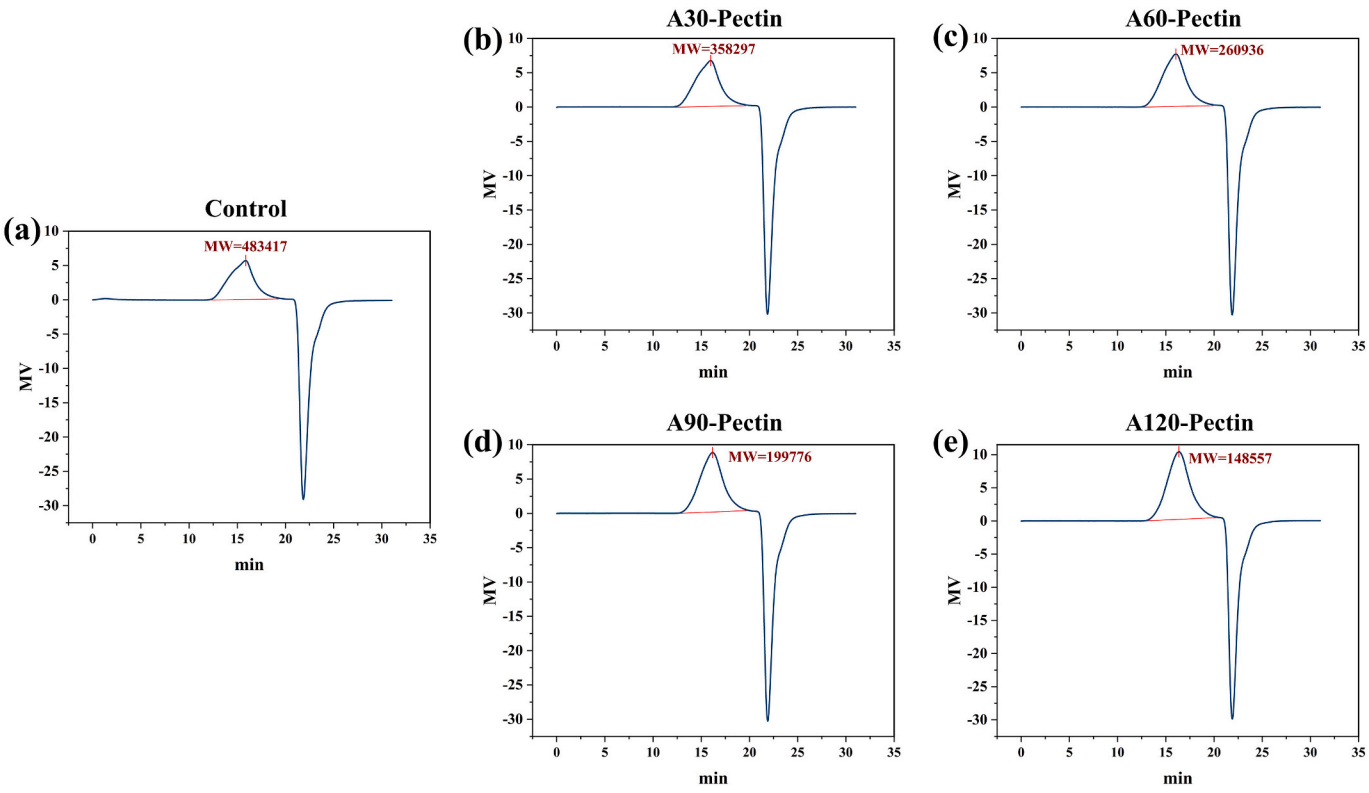

Fig. 2. HPLC chromatogram of APPJ-pectin weight average molecular weight distribution. Control: Natural pectin, A30-Pectin: Pectin treated with APPJ for 30 min, A60-Pectin: Pectin treated with APPJ for 60 min, A90-Pectin: Pectin treated with APPJ for 90 min, A120-Pectin: Pectin treated with APPJ for 120 min.

Table 1
The weight average molecular weight and degree of esterification of APPJ-pectin.

Samples	MW	DE
Control	483,417 Da	57.44%
A30-Pectin	358,297 Da	67.49%
A60-Pectin	260,936 Da	74.08%
A90-Pectin	199,776 Da	84.20%
A120-Pectin	142,557 Da	91.43%

Control: Natural pectin, A30-Pectin: Pectin treated with APPJ for 30 min, A60-Pectin: Pectin treated with APPJ for 60 min, A90-Pectin: Pectin treated with APPJ for 90 min, A120-Pectin: Pectin treated with APPJ for 120 min.

natural pectin. The ester C═O stretching band at 1740 cm^{-1} gradually increased, while the carboxylate C═O stretching band at 1630 cm^{-1} gradually decreased, resulting in a continuous increase in the 1740/1630 peak area ratio with increasing APPJ treatment time. Based on the 1740/1630 peak area ratio, the calculated DE of natural pectin in the control group was 57.44%, which increased to 67.49%, 74.08%, 84.20%, and 91.43% after 30, 60, 90, and 120 min of treatment, respectively. This may be related to the decarboxylation of carboxyl groups by RONS generated during air plasma discharge. In a study by Park et al. (2021), naproxen was treated using the plasma in liquid process, and it was found to effectively degrade naproxen through decarboxylation, demethylation, hydroxylation, and dehydration reactions initiated by ·OH, ultimately producing CO_2 and H_2O. However, the effect of air plasma on polysaccharides was complex. In addition to decarboxylation, carboxyl groups could potentially be converted into hydroxyl, amino (Najah et al., 2022), amide, and other functional groups through the influence of RONS. The specific processes and mechanisms involved are not yet fully understood in current research.

3.1.3. NMR spectra of APPJ-pectin

^{1}H NMR is a technique that analyzes the response of hydrogen atoms in a magnetic field. By examining polysaccharide molecules in D_2O, it provides key information on the monosaccharide composition, linkage types, branching structures, and molecular conformation of the polysaccharides. The ^{1}H NMR spectra are shown in Fig. 3b. These results suggested that APPJ treatment had a significant effect on the molecular structure of natural pectin. Nearly all proton signals assigned to galacturonic acid (GalA) gradually increased with prolonged APPJ treatment time. This may be due to the significant decrease in the MW of APPJ-pectin after APPJ treatment, which likely increased the exposure of hydrogen protons, thereby enhancing the detected signal intensity. Notably, the peak at a chemical shift of 3.720 ppm (corresponding to –OCH_3 of GalA) also increased significantly, indicating that the DE of APPJ-pectin continuously increased with prolonged treatment time. This result was consistent with the FTIR analysis (Fig. 3a). In addition, the H-1 proton signal of GalA was observed at approximately 5.0 ppm in all samples, indicating that GalA in these pectin samples was mainly linked by α-1,4-glycosidic bonds (Li et al., 2022), which was consistent with the typical structural characteristics of natural pectin.

3.1.4. Rheological analysis of APPJ-pectin

Apparent viscosity analysis can reflect the MW, chain conformation, and intermolecular interactions of polymer systems, and its variations are often used to reveal structural differences and rheological properties of materials. The rheological analysis results are shown in Fig. 3c. All samples exhibited a decrease in apparent viscosity with increasing shear rate, displaying typical shear-thinning behavior. The overall apparent viscosity of the APPJ-pectin solution gradually decreased, reflecting a reduction in MW and weakened intermolecular interactions with prolonged APPJ treatment. This differed from the study by Amirabadi, Milani, and Sohbatzadeh (2021) of gum Arabic, where they found that short-duration cold plasma treatment increased the viscosity of gum Arabic dispersions, possibly due to enhanced intermolecular

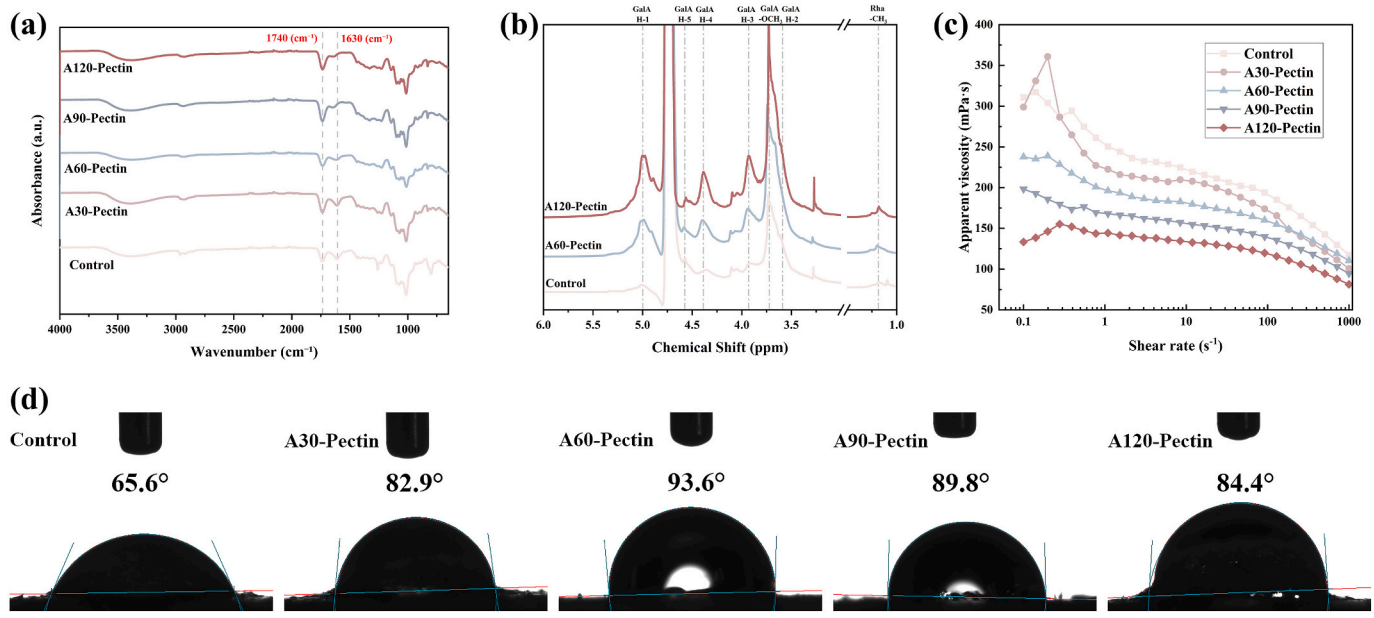

Fig. 3. FTIR spectrum (a), NMR spectrum (b), apparent viscosity (c), and water contact angle (d) of APPJ-pectin.
Control: Natural pectin, A30-Pectin: Pectin treated with APPJ for 30 min, A60-Pectin: Pectin treated with APPJ for 60 min, A90-Pectin: Pectin treated with APPJ for 90 min, A120-Pectin: Pectin treated with APPJ for 120 min.

hydrophobic interactions and hydrogen bonding. They noted that cold plasma treatment increased gum Arabic's hydrophobicity, which was consistent with our study, where the hydrophobicity of APPJ-pectin also increased (Section 3.1.5). However, APPJ-pectin did not exhibit a similar increase in viscosity, which could be attributed to an insufficient enhancement of hydrophobic interactions and hydrogen bonding between pectin molecules, which failed to offset the effect of the decrease in MW. Amirabadi et al. also found that after prolonged treatment, the viscosity of gum Arabic began to decrease continuously, which was consistent with our findings. In addition, in the low shear rate region ($<1\ s^{-1}$), the apparent viscosity of the control and A30-Pectin decreased more rapidly, whereas samples subjected to longer APPJ treatment exhibited a more gradual decrease in this region, suggesting that the susceptibility of the APPJ-pectin solution to low-shear perturbation was reduced.

3.1.5. *Water contact angle of APPJ-pectin*

The water contact angle test measures the contact angle formed by a water droplet on the surface of a dried material, providing insights into its hydrophilicity or hydrophobicity. This method is commonly used to investigate the surface properties of polysaccharide materials and assess their potential applications in the biomedical field. The water contact angle of APPJ-pectin is shown in Fig. 3d. These results indicated that APPJ treatment significantly altered the wettability of APPJ-pectin. Overall, the water contact angle of APPJ-pectin exhibited an initial increase followed by a decrease with prolonged treatment. During the initial stages of APPJ treatment, the increase in the DE of APPJ-pectin led to a higher methoxy content in the molecules, which enhanced its hydrophobicity, resulting in an increase in the contact angle (Sun, Ding, Zhang, Lai, & Chen, 2023). With prolonged APPJ treatment, the MW of APPJ-pectin continued to decrease, and this effect gradually became more pronounced. The increased exposure of molecular segments enhanced the influence of hydrophilic groups, resulting in a gradual decrease in the contact angle. The contact angles of A60-Pectin and A90-Pectin were 93.6° and 89.8°, respectively, indicating evident amphiphilic characteristics.

3.2. *Particle size and zeta potential of APPJ-pectin NPs*

As shown in Fig. 4a, the particle size of APPJ-pectin NPs increased significantly during the initial stages of treatment (A30-Pectin and A60-Pectin) ($p < 0.05$). This phenomenon could be attributed to the increased DE of APPJ-pectin after treatment, which led to a higher methoxy content and enhanced hydrophobicity, thereby strengthening the hydrophobic interactions between pectin molecules, making it easier for them to aggregate and form larger APPJ-pectin NPs. In addition, the absolute value of the Zeta potential (Abs Zeta potential) of APPJ-pectin NPs significantly decreased with prolonged treatment in the initial stages (Fig. 4b). This indicated that some carboxylate groups on the APPJ-pectin molecules were converted to methoxy groups, reducing the negative charge density on the molecular surface (Wan-ling, Jin-song, Jun-Ru, Wen-xin, & Xiao-quan, 2022). The decrease in Abs Zeta potential led to a reduction in electrostatic repulsion between molecules, which further promoted their aggregation. As the APPJ treatment time was extended to 90 min, the particle size of APPJ-pectin NPs began to decrease significantly. The continued decrease in the MW of APPJ-pectin, along with the shortening of molecular chains, weakened its intermolecular interactions and crosslinking ability, leading to the formation of smaller nanoparticles (Luo et al., 2024). The Abs Zeta potential of A90-NPs and A120-NPs increased. After APPJ-pectin degradation, more carboxylate groups were exposed on the molecular surface, enhancing the negative charge density. The increase in Abs Zeta potential further strengthened the electrostatic repulsion between APPJ-pectin molecules, potentially reducing the aggregation tendency. This was one of the key reasons for the decrease in the particle size of APPJ-pectin NPs during this stage.

3.3. *Insulin encapsulation efficiency of APPJ-pectin NPs*

The encapsulation efficiency of APPJ-pectin NPs for insulin showed an overall decreasing trend with the increase in APPJ treatment (Fig. 4c). In the early stages of treatment, the insulin encapsulation efficiency of A30-NPs and A60-NPs showed only a slight decrease ($p > 0.05$). The increase in the DE of APPJ-pectin enhanced its hydrophobicity but decreased the Abs Zeta potential, which weakened the electrostatic interactions with insulin. The strengthened hydrophobic

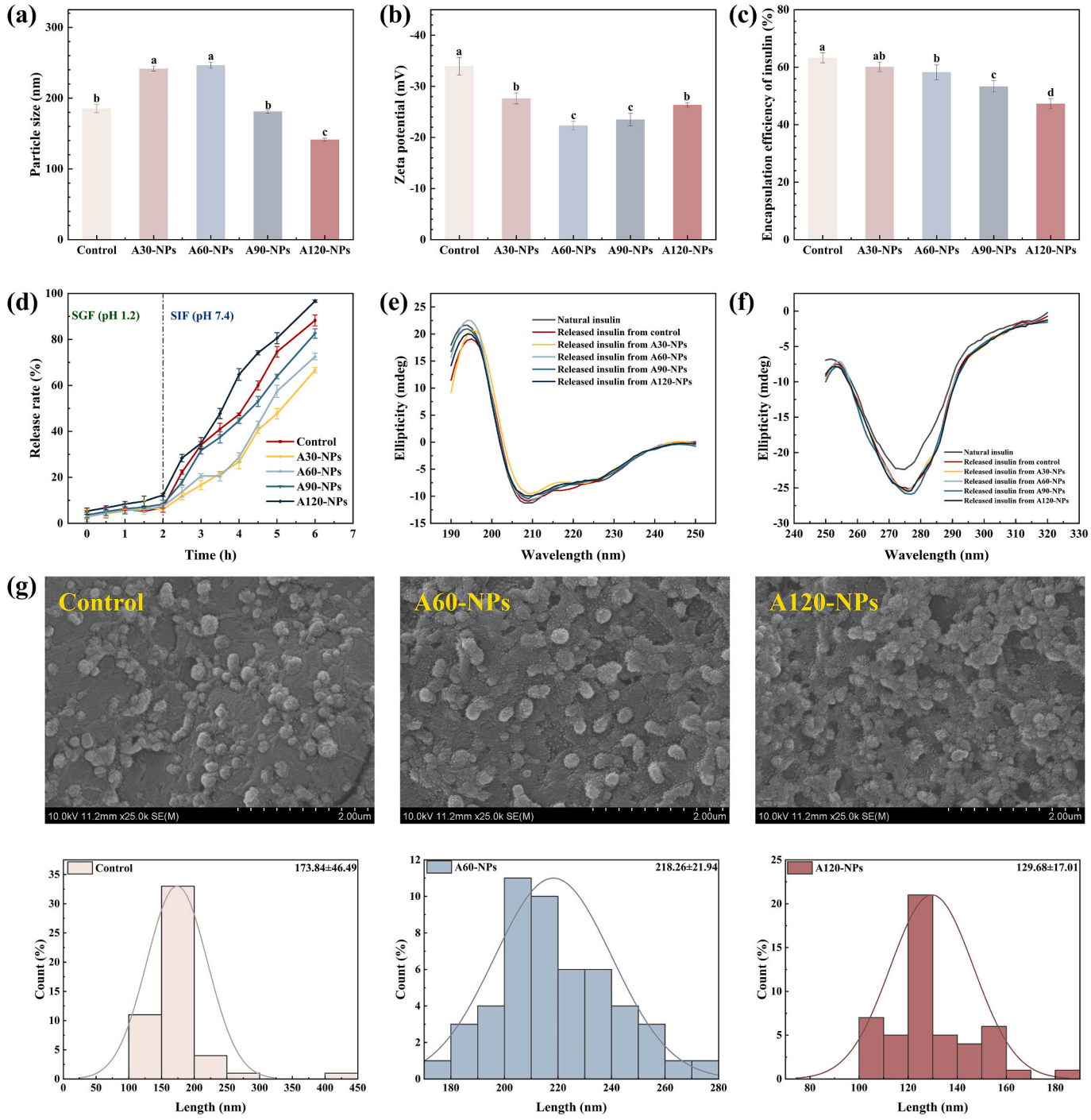

Fig. 4. The particle size (a), Zeta potential (b), insulin encapsulation efficiency (c), and in vitro simulated insulin release (d) of APPJ-pectin NPs. The CD spectroscopy of natural and released insulin (e and f). The SEM images and particle size distribution (g) of APPJ-pectin NPs.
Control: Nanoparticles prepared by encapsulating insulin with natural pectin, A30-NPs: Nanoparticles prepared by encapsulating insulin with A30-Pectin, A60-NPs: Nanoparticles prepared by encapsulating insulin with A60-Pectin, A90-NPs: Nanoparticles prepared by encapsulating insulin with A90-Pectin, A120-NPs: Nanoparticles prepared by encapsulating insulin with A120-Pectin.

interactions partially mitigated this effect, resulting in a slight decrease in encapsulation efficiency. However, the insulin encapsulation efficiency of A90-NPs and A120-NPs decreased significantly ($p < 0.05$). The substantial reduction in the MW of APPJ-pectin weakened its spatial entanglement and crosslinking ability, resulting in a loose or incomplete coating of APPJ-pectin NPs, which significantly reduced the insulin encapsulation efficiency. Furthermore, with prolonged APPJ treatment, the high DE significantly reduced the number of carboxylate groups in APPJ-pectin, weakening the ionic crosslinking between the carboxylate groups and Ca^{2+} (Wang, Munk, Skibsted, & Ahrne, 2022), which further decreased the structural stability of APPJ-pectin NPs, leading to a reduction in insulin encapsulation efficiency.

3.4. *In vitro simulated insulin release of APPJ-pectin NPs*

As shown in Fig. 4d, all APPJ-pectin NPs samples exhibited a slow release of insulin in SGF. Except for A120-NPs, which released 12.29% within 2 h, the release rates of the other samples were all below 10%.

Under acidic conditions, the carboxylate groups in pectin molecules were protonated to form carboxyl groups (–COOH), which weakened the intermolecular electrostatic repulsion and promoted tighter crosslinking, thus imparting higher structural stability to APPJ-pectin NPs. The insulin release rate of all samples significantly increased upon transfer to the SIF environment. At pH 7.4, the carboxyl groups in pectin gradually deprotonated to form carboxylate groups, which enhanced intermolecular electrostatic repulsion and promoted the dissociation of APPJ-pectin NPs (Wang et al., 2023). Furthermore, the overall charge of insulin shifted from positive to negative under this pH, and the interaction between insulin and pectin changed from electrostatic attraction to electrostatic repulsion, further accelerating the release process. In SIF, there were significant differences in the release behavior among the different samples. The insulin release rates of A30-NPs (with the lowest release rate), A60-NPs, and A90-NPs were significantly lower than that of the control group. This may be due to the increased DE of APPJ-pectin, which replaced some carboxylate groups with methoxy groups. Since methoxy groups lack pH responsiveness, the overall pH sensitivity of APPJ-pectin NPs was reduced, thereby slowing down the release of insulin. However, with prolonged APPJ treatment, the release rate of APPJ-pectin NPs gradually increased, and A120-NPs eventually surpassed the control group. The continuous decrease in the MW of APPJ-pectin led to an insufficient chain length to maintain effective spatial entanglement and crosslinking, making APPJ-pectin NPs more prone to dissociation under SIF conditions, thereby accelerating the release of insulin.

3.5. CD spectroscopy of natural and released insulin

As shown in Fig. 4e, the far-UV (190–250 nm) CD spectra revealed that the spectral profiles of natural insulin and all released insulin samples were highly similar. Compared to the known CD spectrum of commercial insulin (Quitério et al., 2021), the experimental results showed a high degree of similarity to the classic insulin spectrum. All samples showed distinct negative peaks at 208 nm (n → π transition) and 222 nm (π → π transition) (Zingale et al., 2023), suggesting that they predominantly contain α-helix structures (Ji et al., 2022). Additionally, all samples exhibited a positive peak at 195 nm, indicating the presence of β-sheet structures (Korpela, Pitkanen, & Heinonen, 2022). Secondary structure analysis based on CD spectra indicated that the differences in content of α-helix, β-sheet, β-turn, and random coil between natural insulin and all released insulin samples were less than 2% (Table 2). The results indicated that both control NPs and APPJ-pectin NPs maintained insulin's secondary structure during encapsulation and release, with no significant changes.

The near-UV (250–320 nm) CD spectrum of insulin is shown in Fig. 4f. Compared to natural insulin, the intensity of the negative peak at 275 nm was slightly increased in the released insulin. This may be related to changes in the local environment of tyrosine residues (Korpela et al., 2022), suggesting that the exposure of insulin's amino acids slightly increased during encapsulation and release. Additionally, pectin in the solution may have interacted with insulin, potentially influencing the exposure of insulin's amino acids. However, the overall profiles of the near-UV CD spectra of natural insulin and released insulin were similar, indicating that the tertiary structure of insulin remained stable during encapsulation and release. The near-UV CD spectra of insulin released from the control NPs and APPJ-pectin NPs nearly overlapped, indicating that the encapsulation and release of insulin by APPJ-pectin NPs did not significantly affect the stability of its tertiary structure. In conclusion, neither control NPs nor APPJ-pectin NPs significantly affected the secondary and tertiary structures of insulin during encapsulation and release, which helped preserve both its structure and biological activity.

Table 2
The secondary structure of natural and released insulin.

Samples	α-helix	β-sheet	β-turn	random coil
Natural insulin	42.8%	21.1%	17.4%	18.8%
Released insulin from control	41.7%	20.5%	17.2%	20.5%
Released insulin from A30-NPs	40.9%	22.3%	17.7%	19.3%
Released insulin from A60-NPs	41.4%	21.7%	17.8%	19.2%
Released insulin from A90-NPs	41.6%	21.2%	17.0%	20.2%
Released insulin from A120-NPs	41.8%	20.7%	18.1%	19.6%

3.6. SEM

The SEM images and particle size distribution are shown in Fig. 4g. All samples successfully formed nanoparticles, with particle sizes predominantly around 200 nm. Compared to the control group, A60-NPs exhibited larger particle sizes and a clearer profile, indicating a more stable structure. This was primarily attributed to the higher DE of A60-Pectin. Arias, Rodríguez, López, and Méndez (2021) prepared nanoparticles using pectin with different DE and found that the nanoparticles formed from high-DE pectin (76.7%) had a significantly larger particle size (255 nm) compared to those formed from low-DE pectin (33.1%, 153 nm). Typically, the lower the MW of polysaccharides, the smaller the particle size of the nanoparticles prepared from them (Villegas-Peralta et al., 2021). Since the prolonged APPJ treatment significantly reduced the MW of A120-Pectin, the particle size of A120-NPs correspondingly decreased, and the morphology became more irregular after drying.

3.7. Hemocompatibility of APPJ-pectin NPs

As shown in Fig. 5, the hemolysis rate of APPJ-pectin NPs increased initially and then decreased with prolonged treatment, with A60-NPs exhibiting the highest hemolysis rate (4.88%). In the early stages of treatment, the increased DE of APPJ-pectin enhanced its hydrophobicity, strengthened the hydrophobic interactions between A30-NPs, A60-NPs, and the lipid hydrophobic regions of the red blood cell membrane, which intensified the membrane integrity disruption. At the same time, these samples exhibited relatively large particle sizes, resulting in more pronounced physical interactions when in contact with the cell membrane. Furthermore, due to the lower Abs Zeta potential of A30-NPs and A60-NPs, the electrostatic repulsion between the negatively charged red blood cell membrane and the APPJ-pectin NPs was weakened, leading to an increased adsorption of these nanoparticles onto the red blood cell membranes. This adsorption process established a strong affinity between the nanoparticles and the red blood cell membranes, involving hydrogen bonding and van der Waals forces (Cai et al., 2025). This interaction induced deformation of the membrane, enabling it to cover more nanoparticle surfaces and generate a driving force that exceeded the hydrophobic interactions between the phospholipids of the cell membrane, ultimately leading to membrane rupture (Wei et al., 2015). With prolonged treatment, the decrease in MW of APPJ-pectin led to a reduction in the particle size of APPJ-pectin NPs. At the same time, the enhanced hydrophilicity weakened their interaction with the hydrophobic regions of the cell membrane. The increase in Abs Zeta potential enhanced the electrostatic repulsion between APPJ-pectin NPs and the red blood cell membrane, which reduced their contact probability with the membrane, ultimately contributing to a decrease in the hemolysis rate. In addition, no significant cytotoxic effects were observed in the pectin solution treated with APPJ (Fig. S1). Overall, the hemolysis rate of all samples ranged from 2% to 5%, suggesting that APPJ-pectin NPs exhibit good biocompatibility.

3.8. Morphological observation of Caco-2 cells

The morphology of Caco-2 cells is presented in Fig. 6a. Caco-2 cells showed typical time-dependent growth and differentiation characteristics during continuous culture. On day 2 post-seeding, the cells were

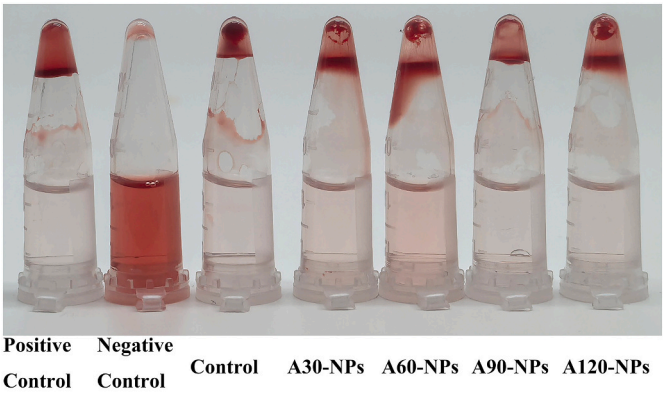

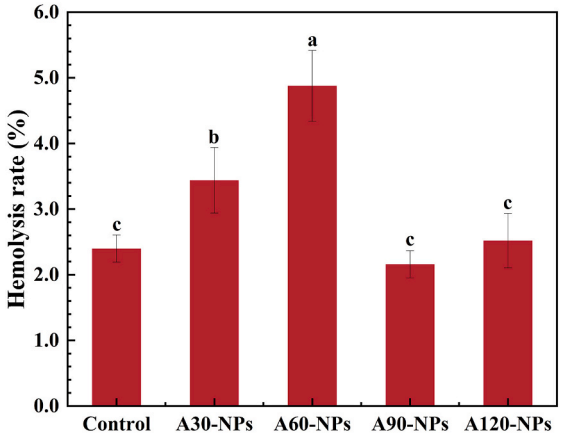

Fig. 5. The hemocompatibility of APPJ-pectin NPs.
Control: Nanoparticles prepared by encapsulating insulin with natural pectin, A30-NPs: Nanoparticles prepared by encapsulating insulin with A30-Pectin, A60-NPs: Nanoparticles prepared by encapsulating insulin with A60-Pectin, A90-NPs: Nanoparticles prepared by encapsulating insulin with A90-Pectin, A120-NPs: Nanoparticles prepared by encapsulating insulin with A120-Pectin.

predominantly attached and began to enter the proliferative phase. By day 4, the cells exhibited a colony-like distribution and formed clustered arrangements, with clear boundaries between them, which displayed typical early proliferative morphology. By day 7, the cells had clearly expanded and gradually merged, forming a large cell monolayer with a confluence of approximately 80–90%. By day 11, the culture surface was completely covered by cells, and they gradually adopted a more regular shape, exhibiting a typical cobblestone-like morphology with epithelial characteristics. Additionally, signs of differentiation were observed, such as enhanced intercellular junctions and the formation of a brush border at the apical surface. By day 15, differentiation was more pronounced, polarization was gradually established, and intercellular junctions became tighter. By day 21, differentiation peaked, with nearly all cells displaying a typical epithelial monolayer morphology and a dense brush border, suggesting that the Caco-2 cells had established a mature intestinal epithelial barrier model.

3.9. Transepithelial cells study of APPJ-pectin NPs in vitro

After oral administration, the insulin delivery system usually enters the bloodstream via the transcellular pathway or the paracellular route through tight junctions between epithelial cells. Once the delivery system successfully crosses the intestinal epithelium, it enters the portal system, where it releases insulin. The insulin is then transported to the liver via the bloodstream, where it regulates blood glucose levels (Chellathurai et al., 2023). To simulate this process, the Transwell system (the system effectively simulates the structure and function of the intestinal epithelium) was used to assess the transport capability of APPJ-pectin NPs across intestinal epithelial cells (Fig. 6b) (Hu, Li, Huang, Wang, & Han, 2021).

In the concentration range of 0 to 15 μg/mL, the fluorescence intensity of FITC exhibited a strong linear correlation with its concentration (Fig. 6c). The calculations resulted in a labeling efficiency of ins-FITC at 3.036%, expressed as the mass ratio of FITC to labeled insulin.

As shown in Fig. 6d, e, and f, the transepithelial transport efficiency of APPJ-pectin NPs exhibited different trends with varying incubation times. The apparent permeability coefficient (Papp) of all samples was low, with little variation observed after 30 min of incubation. This was because Caco-2 cells had taken up APPJ-pectin NPs, but they had not yet been transported into the basolateral chamber (BL) and had remained inside the cells. As the incubation time was extended to 30–60 min, the Papp levels of all samples increased overall, with a more pronounced variation observed between them. The Papp of APPJ-pectin NPs generally increased, with the A60-NPs exhibiting the highest Papp. The increased hydrophobicity of APPJ-pectin NPs and the decrease in Abs Zeta potential enhanced the interaction between APPJ-pectin NPs and the cell membrane (Zheng et al., 2024), facilitating their transepithelial transport. After 60–90 min of incubation, the Papp trend remained similar across all samples, but the overall Papp levels decreased. This was attributed to the decrease in the concentration of APPJ-pectin NPs in the apical chamber (AP), resulting in a reduction in transport efficiency. At this stage, A120-NPs exhibited the lowest Papp. This could be due to the excessive reduction in the MW of A120-pectin, which caused its molecular chains to become too short, thereby weakening the formation of a stable three-dimensional network. Bruinsmann et al. (2019) prepared lipid-core nanoparticles coated with chitosan of different MW for simvastatin nasal delivery. They found that the nanocapsules prepared with low MW chitosan (21 kDa) exhibited a higher drug release rate compared to those prepared with high MW chitosan (152 kDa). Our results were consistent with theirs, as A120-NPs demonstrated a faster insulin release rate (Section 3.4), releasing more insulin-FITC before transepithelial transport. Due to the hydrophilicity, negative charge, and macromolecular structure of insulin, these characteristics made it difficult for insulin to continue crossing the epithelial cell layer after release in the intestine, thus limiting its further absorption. Ultimately, these factors led to a reduced transepithelial transport efficiency of A120-NPs.

3.10. Evaluation of APPJ-pectin NPs uptake by Caco-2 cells

3.10.1. CLSM observation

The intensity of green fluorescence (ins-FITC) observed using CLSM provided a direct indication of the uptake efficiency and distribution of APPJ-pectin NPs in Caco-2 cells. As shown in Fig. 7, the green fluorescence of the cell samples treated with APPJ-pectin NPs increased initially and then decreased. The cell samples treated with A60-NPs exhibited the strongest green fluorescence, suggesting a higher uptake of A60-NPs in Caco-2 cells. The decrease in the Abs Zeta potential of A60-NPs led to a reduction in the surface negative charge density, which in turn weakened the electrostatic repulsion between A60-NPs and the negatively charged cell membrane (Ray & Ray, 2023), thereby increasing the contact between A60-NPs and the cell membrane. In addition, the increased DE of A60-pectin enhanced the surface hydrophobicity of A60-NPs, allowing for stronger hydrophobic interactions between the A60-NPs and the hydrophobic regions of the lipid bilayer, thereby promoting their internalization by the cells (Luo et al., 2025). However, the green fluorescence of cell samples treated with A120-NPs was similar to that in the control group, indicating a decreased uptake of A120-NPs by the cells. This may be attributed to the increased hydrophilicity and the recovery of Abs Zeta potential of A120-NPs, which weakened their interaction with the cell membrane. Moreover, the faster insulin release rate of A120-NPs under neutral pH may have led to the release of more ins-FITC before it was taken up by Caco-2 cells, thereby

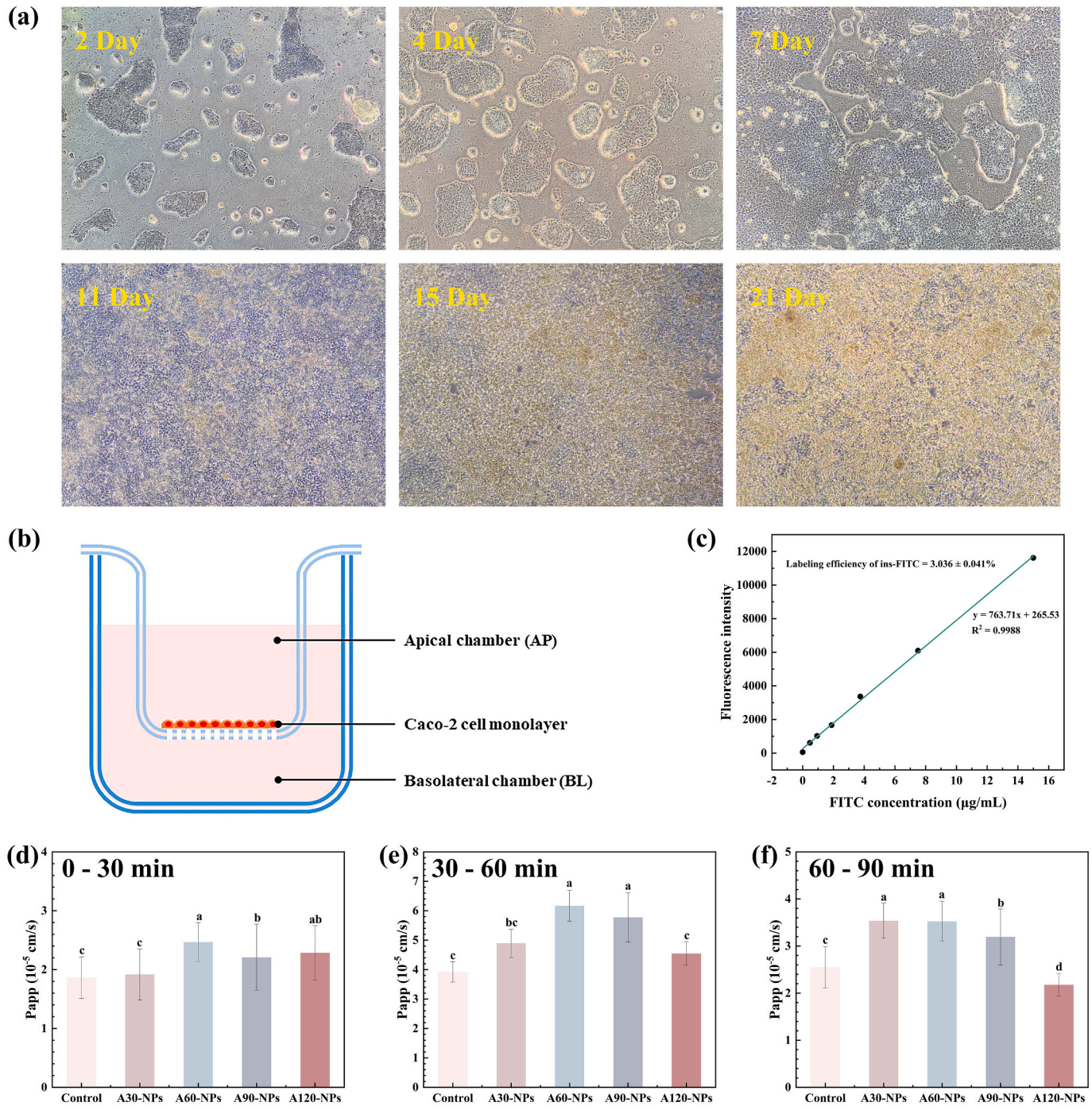

Fig. 6. The morphological observation of Caco-2 cells (a). Schematic diagram of the Transwell system (b). Standard curve of FITC concentration versus fluorescence intensity (c). The transepithelial transport efficiency of APPJ-pectin NPs: 0–30 min (d), 30–60 min (e), 60–90 min (f).
Control: Nanoparticles prepared by encapsulating insulin with natural pectin, A30-NPs: Nanoparticles prepared by encapsulating insulin with A30-Pectin, A60-NPs: Nanoparticles prepared by encapsulating insulin with A60-Pectin, A90-NPs: Nanoparticles prepared by encapsulating insulin with A90-Pectin, A120-NPs: Nanoparticles prepared by encapsulating insulin with A120-Pectin.

affecting the accumulation of FITC inside the cells.

3.10.2. Flow cytometric analysis

The histogram of FITC-A fluorescence intensity in Caco-2 cells is shown in Fig. 8. The fluorescence intensity of all samples increased with prolonged incubation time, indicating that APPJ-pectin-FITC NPs were gradually internalized by the cells. After 0.5 h of incubation, the percentages of FITC-positive cells in the control, A60-NPs, and A120-NPs treated samples were 19.6%, 82.2%, and 26.1%, respectively. At this time, the uptake of A60-NPs by the cells was significantly higher than that of the other groups. After 1.5 h of incubation, the percentage of FITC-positive cells in all samples exceeded 99%, indicating that nearly all cells successfully internalized APPJ-pectin-FITC NPs. Notably, the FITC mean fluorescence intensity (MFI) of the A60-NPs treated samples was 12,458, significantly higher than that of the control (8605) and A120-NPs (7236) treated samples, further indicating a higher internalization efficiency of A60-NPs in Caco-2 cells. The results of flow cytometric analysis were consistent with those observed in CLSM.

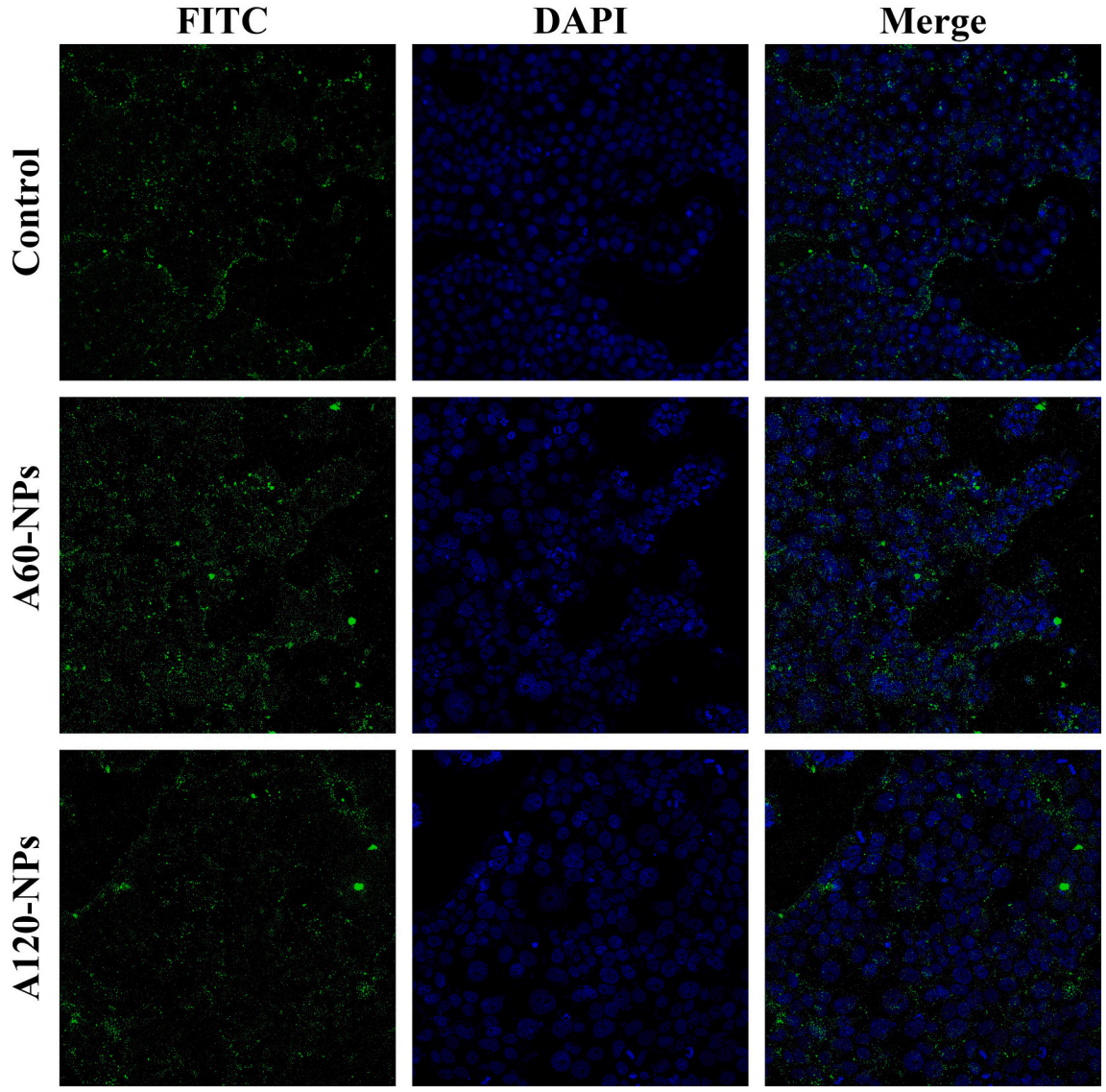

Fig. 7. The CLSM analysis of Caco-2 cell uptake of APPJ-pectin NPs.
Control: Nanoparticles prepared by encapsulating insulin with natural pectin, A60-NPs: Nanoparticles prepared by encapsulating insulin with A60-Pectin, A120-NPs: Nanoparticles prepared by encapsulating insulin with A120-Pectin.

3.11. Investigation of the transepithelial transport mechanism of APPJ-pectin NPs

3.11.1. Paracellular pathway of APPJ-pectin NPs in transepithelial transport

The main routes of nanoparticles transepithelial transport are the transcellular and paracellular pathways (Fig. 9a), both of which play crucial roles in the intestinal absorption of nanoparticles. The transcellular pathway refers to the direct route through intestinal epithelial cells. Upon contact with the epithelial surface, nanoparticles are internalized via endocytosis. Following internalization, they undergo intracellular transport, where they may be routed through the endoplasmic reticulum (ER) and the Golgi apparatus, ultimately being exocytosed at the basolateral membrane into the bloodstream. The paracellular pathway involves nanoparticles temporarily opening the tight junctions between intestinal epithelial cells, allowing the nanoparticles to pass through the intercellular spaces and enter the bloodstream.

TEER testing evaluates the functionality of tight junctions by measuring the resistance of the cell monolayer. When tight junctions are disrupted, the TEER of the cell monolayer decreases, indicating increased permeability of the intercellular spaces, which facilitates the passage of nanoparticles through the paracellular pathway into the bloodstream. As shown in Fig. 9b, the TEER of the control (untreated) sample remained consistently around 800 $\Omega \cdot cm^2$, indicating that the Caco-2 cells successfully formed a complete and stable monolayer during the culture process. After treatment with APPJ-pectin NPs (time $\leq$ 2 h), the TEER of all samples showed a slight decrease, suggesting that APPJ-pectin NPs potentially affected the barrier function of the cell monolayer. This change could be related to a temporary relaxation and increased permeability of the tight junctions between the cells. However, the TEER of all samples rapidly recovered after treatment, almost returning to the level of the control (untreated) sample within 3 h. This suggested that the effect was mild and transient, without causing significant long-term damage to the integrity of the cell monolayer.

Zonula Occludens-1 (ZO-1, tight junction protein) plays a critical role in reflecting the integrity of tight junctions through its distribution between Caco-2 cells. By observing the fluorescence intensity and distribution of ZO-1 in intercellular spaces via immunofluorescence staining, it is possible to verify whether nanoparticles induce the disruption of tight junctions, thus confirming whether nanoparticles are

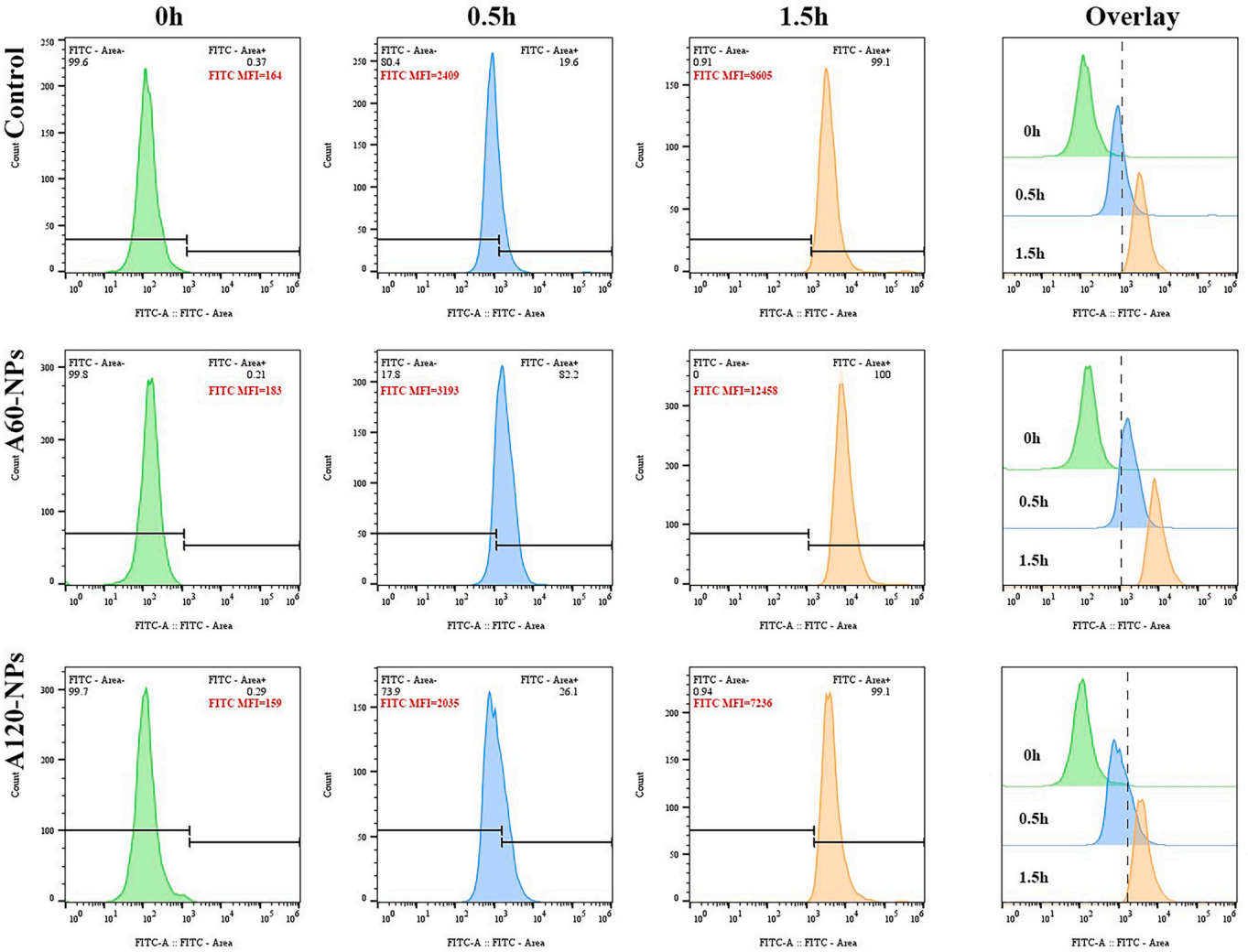

Fig. 8. The flow cytometry histograms of Caco-2 cell uptake of APPJ-pectin NPs.
Control: Nanoparticles prepared by encapsulating insulin with natural pectin, A60-NPs: Nanoparticles prepared by encapsulating insulin with A60-Pectin, A120-NPs: Nanoparticles prepared by encapsulating insulin with A120-Pectin.

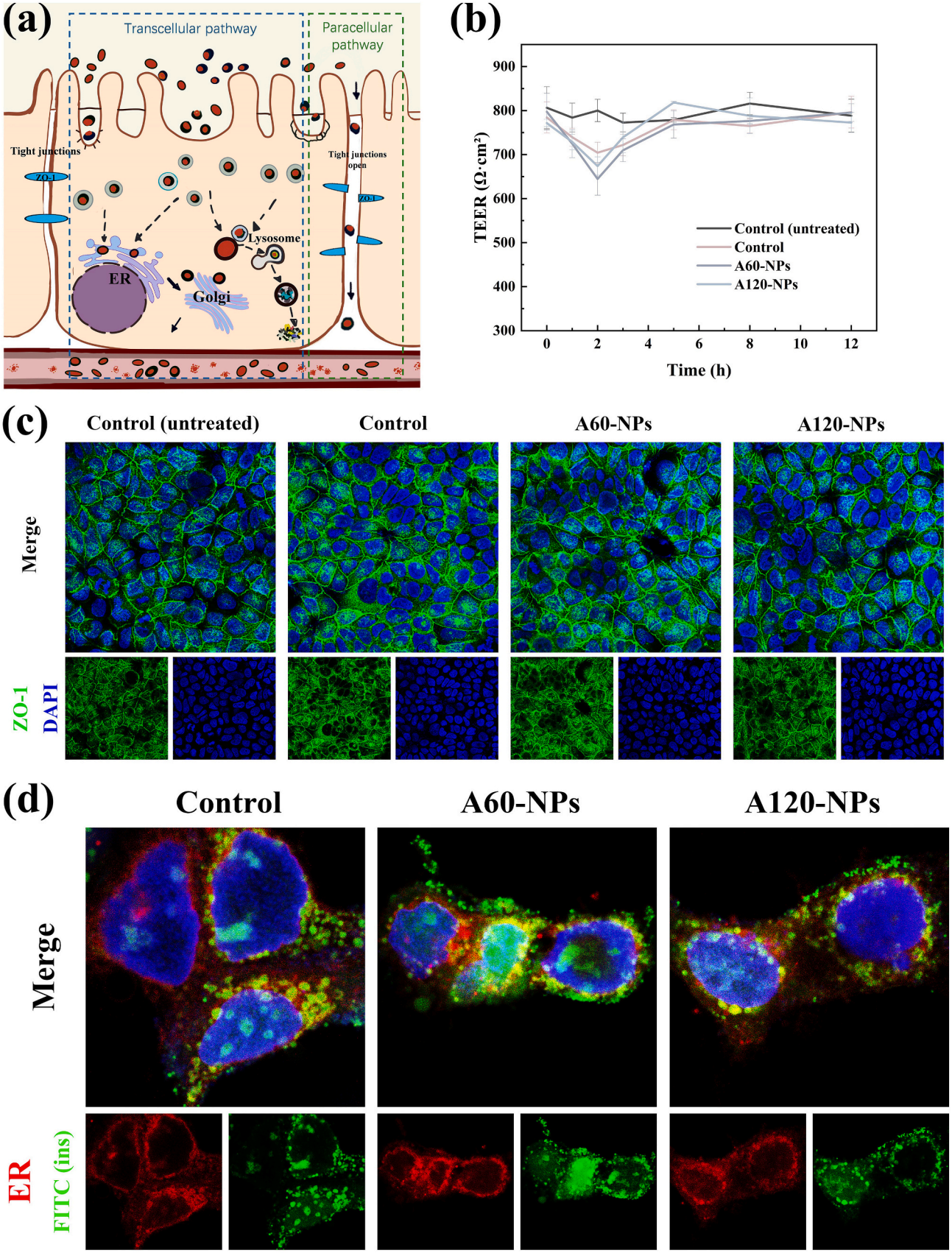

Fig. 9. Schematic of the transepithelial transport mechanism of nanoparticles (a). TEER of Caco-2 cell monolayers treated with APPJ-pectin NPs (b). Immunofluorescence staining of tight junction protein ZO-1 treated with APPJ-pectin NPs (c). Co-localization of ER and APPJ-pectin-FITC NPs in Caco-2 cells (d).
Control: Nanoparticles prepared by encapsulating insulin with natural pectin, A60-NPs: Nanoparticles prepared by encapsulating insulin with A60-Pectin, A120-NPs: Nanoparticles prepared by encapsulating insulin with A120-Pectin.

transported via the paracellular pathway. As shown in Fig. 9c, the bright filamentous green fluorescence between Caco-2 cells represented ZO-1. In the control (untreated) sample, the green fluorescence of ZO-1 was evenly distributed between the cells, indicating the intact tight junctions and the well-formed cell monolayers. After treatment with APPJ-pectin NPs, ZO-1 green fluorescence was only weakened in a few areas, without complete disappearance, which indicated that the tight junctions between cells were only mildly disrupted. This could have been due to localized oxidative stress induced by the uptake of APPJ-pectin NPs by the cells, which might have affected the structure and stability of ZO-1. In comparison, the cells demonstrated a higher uptake of A60-NPs, resulting in a more pronounced reduction in the ZO-1 fluorescence signal. Moreover, Liu et al. (2026) found that β-lactoglobulin nanofibers could induce the influx of Ca^{2+}. The increase in intracellular Ca^{2+} activated calpain. This enzyme cleaved tight junction proteins, which in turn increased paracellular permeability, thereby promoting the absorption of therapeutic peptides such as insulin. Similarly, Ca^{2+} were added during the preparation of APPJ-pectin NPs for ionic crosslinking. After entering the cells, these nanoparticles also increased intracellular Ca^{2+} concentration, activating a similar paracellular permeability regulation mechanism. Overall, APPJ-pectin NPs had a slight impact on the integrity of the Caco-2 cell monolayer, suggesting that the paracellular pathway was not the primary mechanism for their transepithelial transport.

3.11.2. Transcellular pathway of APPJ-pectin NPs in transepithelial transport

In all samples, the distribution of green fluorescence (APPJ-pectin NPs) and red fluorescence (ER) within the cells showed pronounced fluorescence overlap, suggesting that APPJ-pectin NPs were extensively internalized by Caco-2 cells and significantly co-localized with the ER (Fig. 9d). This observation suggested that APPJ-pectin NPs primarily underwent transepithelial transport via the transcellular pathway. Specifically, APPJ-pectin NPs were initially internalized via endocytosis after contacting Caco-2 cells. Subsequently, the APPJ-pectin NPs underwent intracellular transport, possibly via the ER-Golgi secretion pathway, and were eventually released into the bloodstream at the basolateral membrane.

4. Conclusions

This study investigated the effects of APPJ treatment on pectin and its nanoparticles, and evaluated their potential for oral insulin delivery. The results showed that APPJ treatment significantly reduced the MW of pectin and increased its DE. The water contact angle variation indicated that APPJ treatment altered the hydrophilicity and hydrophobicity of pectin, resulting in amphiphilic characteristics. The insulin encapsulation efficiency of APPJ-pectin NPs decreased slightly after treatment, with a more significant decline after 90 min (A90-NPs, A120-NPs). This might have been due to significant degradation of APPJ-pectin molecules, weakening the structural stability of the nanoparticles. In vitro release studies showed that insulin was released slowly from APPJ-pectin NPs in SGF. At neutral pH, the release rate was overall accelerated. After APPJ treatment, the release rate decreased initially before increasing, with A120-NPs showing the fastest rate. CD spectroscopy confirmed that APPJ-pectin NPs preserved insulin's secondary and tertiary structures during encapsulation and release, ensuring its biological activity throughout. Although the hemolysis rate of APPJ-pectin NPs initially increased, it remained low (2%–5%), demonstrating good hemocompatibility. The APPJ-pectin NPs primarily underwent transepithelial transport via the transcellular pathway, with minimal and transient disruption of tight junctions, suggesting that the paracellular pathway played a secondary role in their absorption. The Transwell system was used to evaluate the transepithelial transport efficiency of APPJ-pectin NPs. The results showed that as treatment time increased, Papp first increased and then decreased, with A60-NPs exhibiting the highest Papp. CLSM observation and flow cytometry analysis further validated the time-dependent uptake of APPJ-pectin NPs by Caco-2 cells. A60-NPs demonstrated significantly higher internalization efficiency than the other groups. In conclusion, APPJ treatment modulated the physicochemical properties of pectin and its nanoparticles, optimizing their performance in oral insulin delivery.

CRediT authorship contribution statement

Nuo Chen: Writing – original draft, Methodology, Formal analysis, Data curation, Conceptualization. **Xijia Zhang:** Software, Resources. **Weichao Cao:** Visualization, Validation. **Hong Tian:** Supervision, Resources. **Xiao Hua:** Writing – review & editing, Project administration, Investigation, Funding acquisition, Conceptualization.

Declaration of competing interest

The authors declare that they have no known competing financial interests or personal relationships that could have appeared to influence the work reported in this paper.

Acknowledgments

This work was supported by the Science and Technology Program of Inner Mongolia (20241125KYY0004, 2024ZY0060), and the Science and Technology Program of Shandong Province (2024TSGC0489, 2024CXFZ09).

Appendix A. Supplementary data

Supplementary data to this article can be found online at https://doi.org/10.1016/j.carbpol.2026.124970.

Data availability

Data will be made available on request.

References

Amirabadi, S., Milani, J. M., & Sohbatzadeh, F. (2021). Effects of cold atmospheric-pressure plasma on the rheological properties of gum Arabic. *Food Hydrocolloids, 117*, Article 106724. https://doi.org/10.1016/j.foodhyd.2021.106724

Arias, D., Rodríguez, J., López, B., & Méndez, P. (2021). Evaluation of the physicochemical properties of pectin extracted from Musa paradisiaca banana peels at different pH conditions in the formation of nanoparticles. *Heliyon, 7*(1), Article e06059. https://doi.org/10.1016/j.heliyon.2021.e06059

Booth, J. P., Mozetic, M., Nikiforov, A., & Oehr, C. (2022). Foundations of plasma surface functionalization of polymers for industrial and biological applications. *Plasma Sources Science & Technology, 31*(10), Article 103001. https://doi.org/10.1088/1361-6595/ac70f9

Bruinsmann, F. A., Pigana, S., Aguirre, T., Souto, G. D., Pereira, G. G., Bianchera, A., & Sonvico, F. (2019). Chitosan-coated nanoparticles: Effect of chitosan molecular weight on nasal Transmucosal delivery. *Pharmaceutics, 11*(2). https://doi.org/10.3390/pharmaceutics11020086. Article 86.

Cai, X. Y., Chen, H. Y., Peng, Z. H., Li, Y., Tan, S., Li, D. Y., & Li, X. Y. (2025). Nano-safety guardians: Surface engineering strategies for building hemocompatible shields. *Applied surface science Advances, 30*, Article 100891. https://doi.org/10.1016/j.apsadv.2025.100891

Chellathurai, M. S., Yong, C. L., Sofian, Z. M., Sahudin, S., Hasim, N. B. M., & Mahmood, S. (2023). Self-assembled chitosan-insulin oral nanoparticles-a critical perspective review. *International Journal of Biological Macromolecules, 243*, Article 125125. https://doi.org/10.1016/j.ijbiomac.2023.125125

Chokradjaroen, C., Rujirayanit, R., Watthanaphanit, A., Theeramunkong, S., Saito, N., Yamashita, K., & Arakawa, R. (2017). Enhanced degradation of chitosan by applying plasma treatment in combination with oxidizing agents for potential use as an anticancer agent. *Carbohydrate Polymers, 167*, 1–11. https://doi.org/10.1016/j.carbpol.2017.03.006

Elsabahy, M., Song, Y., Eissa, N. G., Khan, S., Hamad, M. A., & Wooley, K. L. (2021). Morphologic design of sugar-based polymer nanoparticles for delivery of antidiabetic peptides. *Journal of Controlled Release, 334*, 1–10. https://doi.org/10.1016/j.jconrel.2021.04.006

Fang, Z., Yang, J. R., Liu, Y., Shao, T., & Zhang, C. (2013). Surface treatment of polyethylene terephthalate to improving hydrophilicity using atmospheric pressure

plasma jet. *IEEE Transactions on Plasma Science, 41*(6), 1627–1634. https://doi.org/10.1109/tps.2013.2259508
Gu, X. L., Li, W. B., Jiang, X. Y., Chang, C., & Wu, J. E. (2024). Pectin-coated whey protein isolate/zein self-aggregated nanoparticles as curcumin delivery vehicles: Effects of heating, pH, and adding sequence. *International Journal of Biological Macromolecules, 258*, Article 128892. https://doi.org/10.1016/j.ijbiomac.2023.128892
Hu, M. X., Li, Y., Huang, J. J., Wang, X., & Han, J. Z. (2021). Electrospun scaffold for biomimic culture of Caco-2 cell monolayer as an In vitro intestinal model. *ACS Applied Bio Materials, 4*(2), 1340–1349. https://doi.org/10.1021/acsabm.0c01230
Hu, W. Z., Li, P., Guo, D. X., Zhang, B. Q., Tao, D. B., Li, J. F., & Ma, F. M. (2023). Effect of solution pulsed plasma process on the degradation and physicochemical properties of pectin. *Food Hydrocolloids, 136*, Article 108236. https://doi.org/10.1016/j.foodhyd.2022.108236
Huo, Q. Q., Zhou, J., Tang, H., Wu, W. B., Hu, S., Dong, E. P., & Liu, D. F. (2023). Nanoparticle surface decoration mediated efficient protein and peptide co-encapsulation with precise ratiometric control for self-regulated drug release. *Nanoscale, 15*(10), 5063–5073. https://doi.org/10.1039/d2nr05744a
Ji, Y. M., Zhang, W. Y., Zhang, J. D., Li, X. F., Yu, F. D., Li, C. Y., & Xing, G. W. (2022). Dual functional amphiphilic sugar-coated AIE-active fluorescent organic nanoparticles for the monitoring and inhibition of insulin amyloid fibrillation based on carbohydrate-protein interactions. *Journal of Materials Chemistry B, 10*(29), 5602–5611. https://doi.org/10.1039/d2tb01070d
Joshi, D., Aghara, H., Patel, H., Suthar, S., Mandal, P., Patel, D., & Kikani, B. (2025). Evaluating the potential of Halomonas pacifica DJ6.1 L-asparaginase: Statistical production optimization, biochemical characterization and anticancer attributes using Caco-2 cell lines. *International Journal of Biological Macromolecules, 311*, Article 143723. https://doi.org/10.1016/j.ijbiomac.2025.143723
Korpela, B., Pitkanen, L., & Heinonen, M. (2022). Enzymatic modification of oat globulin enables covalent interaction with procyanidin B2. *Food Chemistry, 395*, Article 133568. https://doi.org/10.1016/j.foodchem.2022.133568
Lamson, N. G., Berger, A., Fein, K. C., & Whitehead, K. A. (2020). Anionic nanoparticles enable the oral delivery of proteins by enhancing intestinal permeability. *Nature Biomedical Engineering, 4*(1), 84–96. https://doi.org/10.1038/s41551-019-0465-5
Li, G., Wang, F., Wang, M. M., Tang, M. T., Zhou, T., & Gu, Q. (2022). Physicochemical, structural and rheological properties of pectin isolated from citrus canning processing water. *International Journal of Biological Macromolecules, 195*, 12–21. https://doi.org/10.1016/j.ijbiomac.2021.11.203
Libo, W., Fangming, W., Yinzhao, G., Zhe, C., Yanhui, W., & Yaqin, X. (2024). Construction and characterization of selenium nanoparticles stabilized by cranberry polyphenols with protective effects on erythrocyte hemolysis. *Food. Bioscience, 61*, Article 104925. https://doi.org/10.1016/j.fbio.2024.104925
Liu, X., Li, S., Wu, G., Jia, W., Zhao, Y., Fang, Y., & Cao, Y. (2026). Food-derived beta-lactoglobulin nanofibrils: An efficacy, safe, and scalable solution to overcome oral insulin delivery challenges. *Bioactive Materials, 57*, 646–659. https://doi.org/10.1016/j.bioactmat.2025.11.020
Liu, Y., Li, D. R., Chen, M. N., Sun, Q. Y., Zhang, Y., Zhou, J., & Wang, T. C. (2023). Radical adducts formation mechanism of CH_3CO_2 and CH_3CO_3 realized decomposition of chitosan by plasma catalyzed peracetic acid. *Carbohydrate Polymers, 318*, Article 121121. https://doi.org/10.1016/j.carbpol.2023.121121
Low, C. Y., Gan, W. L., Lai, S. J., Tam, R. S. M., Tan, J. F., Dietl, S., & Bakhtiar, A. (2025). Critical updates on oral insulin drug delivery systems for type 2 diabetes mellitus. *Journal of Nanobiotechnology, 23*(1). https://doi.org/10.1186/s12951-024-03062-7. Article 16.
Luo, F. J., Zhang, Z. Y., Lu, F. Q., Li, D. J., Zhou, C. S., Li, Y., & He, W. W. (2024). Ultrasound modification of pectin and the mechanism of its interaction with cyanidin-3-O-glucoside. *Food Hydrocolloids, 152*, Article 109898. https://doi.org/10.1016/j.foodhyd.2024.109898
Luo, T. K., Kim, Y. J., Cushing, A., Ma, Y. L., Han, Z. Y., Johnson, R. E., & Mirkin, C. A. (2025). Cleavable hydrophobic anchors optimize immunomodulatory effects of oligonucleotides. *Journal of the American Chemical Society, 147*(42), 38907–38921. https://doi.org/10.1021/jacs.5c15110
Lv, B. W., Shang, K. F., Lu, N., Yang, Z. T., & Guo, L. (2025). Generation of reactive species and sulfamethoxazole degradation in a surface packed-bed discharge reactor. *Plasma Processes and Polymers, 22*(5), Article 2400272. https://doi.org/10.1002/ppap.202400272
Matra, K., Aryuwong, W., Meetang, W., Ruthairat, S., Dechthummarong, C., Sangwang, W., & Luang-In, V. (2023). Application of electrical breakdown in liquid process on inulin structural transformations. *IEEE Access, 11*, 114777–114789. https://doi.org/10.1109/access.2023.3321339
Nabila, F. H., Islam, R., Yamin, L., Yoshirou, K., Wakabayashi, R., Kamiya, N., & Goto, M. (2024). Transdermal insulin delivery using ionic liquid-mediated Nanovesicles for diabetes treatment. *ACS Biomaterials Science & Engineering, 11*(1), 402–414. https://doi.org/10.1021/acsbiomaterials.4c02000
Najah, A., Boivin, D., Noël, C., De Poucques, L., Henrion, G., & Cuynet, S. (2022). Amino-grafting pre-functionalization of terephthalic acid by impulse dielectric-barrier discharge (DBD) plasma for amino-based metal-organic frameworks (MOFs). *Materials Chemistry and Physics, 290*, Article 126629. https://doi.org/10.1016/j.matchemphys.2022.126629
Ogle, G. D., Wang, F., Haynes, A., Gregory, G. A., King, T. W., Deng, K., … Maniam, J. (2025). Global type 1 diabetes prevalence, incidence, and mortality estimates 2025: Results from the international diabetes federation atlas, 11th edition, and the T1D index version 3.0. *Diabetes research and clinical practice, 225*, Article 112277. https://doi.org/10.1016/j.diabres.2025.112277
Park, Y. K., Kim, B. J., Kim, S. C., You, C. S., Choi, J., Park, J., & Jung, S. C. (2021). Decomposition of naproxen by plasma in liquid process with TiO2 photocatslysts and hydrogen peroxide. *Environmental Research, 195*, Article 110899. https://doi.org/10.1016/j.envres.2021.110899
Pei, Y. H., Zhang, Z. H., Duan, Z. H., Gao, T., Jiang, Q. Y., Hu, S. L., & Yuan, M. (2024). Preparation and characterization of high-methoxyl pectin/glycerides emulsion for pH-responsive, targeting, and sustained release of fat-soluble substances. *International Journal of Biological Macromolecules, 282*, Article 136675. https://doi.org/10.1016/j.ijbiomac.2024.136675
Quitério, M., Simoes, S., Ascenso, A., Carvalheiro, M., Leandro, A. P., Correia, I., & Reis, C. P. (2021). Development of a topical insulin polymeric Nanoformulation for skin burn regeneration: An experimental approach. *International Journal of Molecular Sciences, 22*(8), Article 4087. https://doi.org/10.3390/ijms22084087
Ray, L., & Ray, S. (2023). Enhanced anticancer activity of siRNA and drug codelivered by anionic biopolymer: Overcoming electrostatic repulsion. *Nanomedicine, 18*(11), 855–874. https://doi.org/10.2217/nnm-2022-0225
Sangwanna, S., Seelarat, W., Panklai, T., Chaosuan, N., Subcharoen, A., Subcharoen, N., & Porjai, P. (2023). Air atmospheric pressure plasma jet to improve fruiting body production and enhance bioactive phytochemicals from mutant Cordyceps militaris (white Cordyceps militaris). *Food and Bioprocess Technology, 16*(9), 1976–1991. https://doi.org/10.1007/s11947-023-03028-x
Seelarat, W., Sangwanna, S., Chaiwon, T., Panklai, T., Chaosuan, N., Bootchanont, A., & Boonyawan, D. (2024). Impact of pretreatment with dielectric barrier discharge plasma on the drying characteristics and bioactive compounds of jackfruit slices. *Journal of the Science of Food and Agriculture, 104*(6), 3654–3664. https://doi.org/10.1002/jsfa.13250
Shang, K. F., Morent, R., De Geyter, N., Wang, Y. X., & Yang, Z. T. (2025). Plasma catalytic degradation of sulfamethoxazole in water with Fe/ Mn-LDO catalyst: Performance and mechanism. *Separation and Purification Technology, 360*, Article 131145. https://doi.org/10.1016/j.seppur.2024.131145
Shiyang, L., Yangguang, L., Mengting, D., Meichao, Z., Zifang, Z., Haohao, W., & Adewale Olusegun, O. (2024). Glycogen and zinc-enriched ferritin as bioavailable nanoparticulate nutrients released from gastrointestinal digestion of pacific oyster (Crassostrea gigas). *Food Chemistry, 457*, Article 140125. https://doi.org/10.1016/j.foodchem.2024.140125
Sun, X. Y., Ding, L., Zhang, L. F., Lai, S. J., & Chen, F. S. (2023). Interaction mechanisms of peanut protein isolate and high methoxyl pectin with ultrasound treatment: The effect of ultrasound parameters, biopolymer ratio, and pH. *Food Chemistry, 429*, Article 136810. https://doi.org/10.1016/j.foodchem.2023.136810
Surucu, S., Masur, K., Sasmazel, H. T., Von Woedtke, T., & Weltmann, K. D. (2016). Atmospheric plasma surface modifications of electrospun PCL/chitosan/PCL hybrid scaffolds by nozzle type plasma jets for usage of cell cultivation. *Applied Surface Science, 385*, 400–409. https://doi.org/10.1016/j.apsusc.2016.05.123
Villegas-Peralta, Y., López-Cervantes, J., Santana, T. J. M., Sánchez-Duarte, R. G., Sánchez-Machado, D. I., Martínez-Macías, M. D., & Correa-Murrieta, M. A. (2021). Impact of the molecular weight on the size of chitosan nanoparticles: Characterization and its solid-state application. *Polymer Bulletin, 78*(2), 813–832. https://doi.org/10.1007/s00289-020-03139-x
Wang, J., Munk, M. B., Skibsted, L. H., & Ahrne, L. M. (2022). Impact of pectin and whey minerals solubilized by lime juice on calcium bioaccessibility in yogurt based snacks. *Food Hydrocolloids, 131*, Article 107817. https://doi.org/10.1016/j.foodhyd.2022.107817
Wang, J. R., Zhao, C. Y., Zhao, S. J., Lu, X. M., Ma, M. Y., & Zheng, J. K. (2023). Gelling properties of lysine-amidated citrus pectins: The key role of pH in both amidation and gelation. *Carbohydrate Polymers, 317*, Article 121087. https://doi.org/10.1016/j.carbpol.2023.121087
Wang, X. R., Sun, H. N., & Mu, T. H. (2024). Materials and structure of polysaccharide-based delivery carriers for oral insulin: A review. *Carbohydrate Polymers, 323*, Article 121364. https://doi.org/10.1016/j.carbpol.2023.121364
Wang, Y. Y., Li, H., Rasool, A., Wang, H. B., Manzoor, R., & Zhang, G. L. (2024). Polymeric nanoparticles (PNPs) for oral delivery of insulin. *Journal of Nanobiotechnology, 22*(1), Article 1. https://doi.org/10.1186/s12951-023-02253-y
Wan-ling, L., Jin-song, L., Jun-Ru, Q., Wen-xin, J., & Xiao-quan, Y. (2022). Physicochemical characteristics and functional properties of high methoxyl pectin with different degree of esterification. *Food Chemistry, 375*, Article 131806. https://doi.org/10.1016/j.foodchem.2021.131806
Wei, X. R., Jiang, W., Yu, J. C., Ding, L., Hu, J. T., & Jiang, G. B. (2015). Effects of SiO2 nanoparticles on phospholipid membrane integrity and fluidity. *Journal of Hazardous Materials, 287*, 217–224. https://doi.org/10.1016/j.jhazmat.2015.01.063
Yang, D. Y., Zhang, S. L., Xu, Q. Y., Lu, S., Xiao, G. X., Zheng, L., & Zhao, M. M. (2025). Production of collagen-derived hydroxyproline (Hyp)-containing di- and tripeptides by brush border membrane enzymes and their absorption characteristics. *Food Research International, 217*, Article 116847. https://doi.org/10.1016/j.foodres.2025.116847
Yang, R., Zhang, J., Huang, J. Q., Wang, X. F., Yang, H. Y., & Jin, Q. R. (2023). Decreased penetration mechanism of ranitidine due to application of sodium Sulfobutyl ether-β-Cyclodextrin. *Pharmaceutics, 15*(11), Article 2593. https://doi.org/10.3390/pharmaceutics15112593
Yuan, D., Niu, Z. C., Zheng, W. Y., Zhao, Q. Z., Zhou, F. B., & Zhao, M. M. (2024). Mind the particle rigidity: Blooms the bioavailability via rapidly crossing the mucus layer and alters the intracellular fate of curcumin. *ACS Nano, 18*(39), 27026–27041. https://doi.org/10.1021/acsnano.4c09838
Zhang, E. R., Zhu, H., Song, B. Y., Shi, Y. J., & Cao, Z. Q. (2024). Recent advances in oral insulin delivery technologies. *Journal of Controlled Release, 366*, 221–230. https://doi.org/10.1016/j.jconrel.2023.12.045
Zheng, J., Wan, L., Zhang, X. W., Cui, B. F., Xu, X. Y., Xia, J. R., & Wang, K. K. (2025). Effects of surface functional modification of mesoporous silica nanoparticles on oral

insulin delivery: A review. *International Journal of Biological Macromolecules, 319*, Article 145703. https://doi.org/10.1016/j.ijbiomac.2025.145703

Zheng, Y. X., Luo, S. Q., Xu, M., He, Q., Xie, J., Wu, J. W., & Huang, Y. (2024). Transepithelial transport of nanoparticles in oral drug delivery: From the perspective of surface and holistic property modulation. *Acta Pharmaceutica Sinica B, 14*(9), 3876–3900. https://doi.org/10.1016/j.apsb.2024.06.015

Zhu, Q. Y., Zhang, C. Q., Gong, J. B., Xu, W. H., Qin, X. G., Zhang, H. Z., & Liu, G. (2024). Enzyme-glycosylated ovalbumin/chitosan oligosaccharide nanoparticles: Simulation of in vitro digestion for the targeted release of vitamin D_3 and application for encapsulation in beverages. *Food Hydrocolloids, 156*, Article 110324. https://doi.org/10.1016/j.foodhyd.2024.110324

Zingale, G. A., Distefano, A., Pandino, I., Tuccitto, N., Oliveri, V., Gaeta, M., & Grasso, G. (2023). Carbon dots as a versatile tool to monitor insulin aggregation. *Analytical and Bioanalytical Chemistry, 415*(10), 1829–1840. https://doi.org/10.1007/s00216-023-04585-y

Zou, J. J., Chen, Q., Phipps, J., Zhao, Y., Qin, X. D., Tai, W. Y., & Tian, J. (2025). Efficient oral insulin delivery with sustained release by folate-conjugated metal-organic framework nanoparticles. *Matter, 8*(3), Article 101948. https://doi.org/10.1016/j.matt.2024.101948